Mg isotope fractionation during continental weathering and low temperature carbonation of ultramafic rocks

Hans C Oskierski, Andreas Beinlich, Vasileios Mavromatis, Mohammednoor Altarawneh, Bogdan Z Dlugogorski

Mg isotope fractionation during continental weathering and low temperature carbonation of ultramafic rocks

Hans C. Oskierski[a,*], Andreas Beinlich[b], Vasileios Mavromatis[c,d], Mohammednoor Altarawneh[a], Bogdan Z. Dlugogorski[a]

[a]*School of Engineering and Information Technology, Murdoch University, 90 South Street, Murdoch WA, 6150, Australia*

[b]*The Institute for Geoscience Research (TIGeR), School of Earth and Planetary Sciences, Curtin University, 6845 Perth, Australia*

[c]*Institute of Applied Geosciences, Graz University of Technology, Rechbauerstraße 12, 8010 Graz, Austria*

[d]*Géosciences Environnement Toulouse (GET), CNRS, UMR 5563, Observatoire Midi-Pyrénées, 14 Av. E. Belin, 31400 Toulouse, France*

*Corresponding author: H.Oskierski@murdoch.edu.au

Abstract

The Mg-isotope systematics of peridotite weathering and low-temperature carbonation have not yet been thoroughly investigated, despite their potential to provide insights into reaction pathways and mechanisms of lithosphere-hydrosphere transfer of Mg and sequestration of CO_2 in carbonate minerals. Here, we present new observations of the evolution of Mg isotope ratios during subtropical ultramafic rock weathering and associated magnesite formation, including the lowest δ^{26}Mg of magnesite reported so far. At the investigated field sites in eastern Australia, the proximity of the ultramafic Mg source rocks and associated magnesite deposits provides boundary conditions that constrain Mg isotope fractionation during low-temperature alteration. Saprolite samples from Attunga, New South Wales, show that weathering of serpentinite is accompanied by Mg loss and formation of secondary Mg-bearing clay minerals. Furthermore, Mg isotope ratios increase systematically with weathering intensity, indicating that incorporation of ^{26}Mg into clay mineral structures controls Mg-isotope fractionation during ultramafic rock weathering. The Mg-bearing clay formed by decomposition of serpentine minerals has a δ^{26}Mg value of ~ 0.35 ‰, which is up to ~ 0.6 ‰ heavier than the ultramafic precursor. In contrast, nodular magnesite hosted in ultramafic rock shows δ^{26}Mg values between -3.26 ‰ and -2.55 ‰ that are significantly lower than those of magnesite and dolomite that formed by hydrothermal alteration of peridotite at higher temperature (δ^{26}Mg = -0.69 ‰ and -0.62 ‰). The strong enrichment of ^{24}Mg in nodular magnesite does not reconcile with simple fractionation during direct precipitation from ultramafic host rock buffered meteoric fluids and instead suggests multiple formation steps involving dissolution and re-precipitation of pre-existing carbonate accompanied by fractionation between species of dissolved Mg. Our data highlight the potential of Mg isotope studies for distinguishing the formation pathways of low temperature magnesite and for tracing Mg in low temperature alteration processes based on the distinct signatures of secondary silicate and carbonate minerals.

1. Introduction

Magnesium isotopes represent a powerful tracer for low-temperature geochemical processes due to significant fractionation during chemical weathering (Brewer et al., 2018; Huang et al., 2012; Lara et al., 2017; Liu et al., 2014; Pogge von Strandmann et al., 2008, 2012; Pokrovsky et al., 2011; Teng et al., 2010a; Tipper et al., 2006a, b, 2012a, b; Wimpenny et al., 2010, 2011), soil formation, uptake by vegetation (Opfergelt et al., 2012, 2014; Mavromatis et al., 2014a; Oelkers et al., 2015; Pokharel et al., 2017) and carbonate mineral formation (e.g. Geske et al., 2012; 2015a; Immenhauser et al., 2010; Mavromatis et al., 2013; Riechelmann et al., 2016; 2018). In comparison, small Mg isotope fractionation is observed during magmatic differentiation (e.g. Dauphas et al., 2010; Li et al., 2011; Liu et al., 2010a; Teng et al., 2010b). This results in a relatively narrow range of Mg isotope ratios in pristine felsic, mafic and ultramafic rocks (~-0.4 ‰ < δ^{26}Mg < ~0.0) in contrast to the strong enrichment of ^{24}Mg in carbonates (with δ^{26}Mg as low as -5.6 ‰; Wombacher et al., 2011) and depletion of ^{24}Mg in weathered silicates (δ^{26}Mg of up to 1.8 ‰; Liu et al., 2014). Variation in magnitude and even direction of Mg isotope fractionation during the formation of secondary silicates has been documented in the literature (Liu et al., 2014; Pogge von Strandmann et al., 2008; 2012; Ryu et al., 2011; Wimpenny et al., 2010; Teng et al., 2010a), e.g. with both lower and higher δ^{26}Mg in saprolites compared to underlying fresh basalt (Huang et al., 2012). This suggests a mineralogical control on Mg isotope fractionation, likely related to Mg-O bond lengths (e.g. Li et al., 2014) but also highlights the influence of adsorption-desorption processes on the Mg isotope composition of weathering residues (Huang et al., 2012; Wimpenny et al., 2014). Accordingly, the Mg budget and thus the Mg isotope composition of clay minerals forming during weathering can be dominated by either structurally bound or labile, adsorbed Mg (Wimpenny et al., 2014; Ryu et al., 2016). As these two Mg fractions are often isotopically distinct (Wimpenny et al., 2014), it is important to consider the actual weathering process (e.g. primary and secondary phase mineralogy, their Mg concentrations, weathering intensity, etc.) to characterise the associated Mg isotope fractionation mechanism.

To better constrain natural fractionation pathways and the influence of the geochemical environment on Mg isotope fractionation between secondary silicate and carbonate phases at low

temperature, we investigate clay mineral-bearing silicate residues and associated magnesite that formed in response to weathering of serpentinised peridotite. Despite the relatively small volume compared to other rock types, peridotite weathering is important for the composition of the bulk continental crust due to its distinct chemical composition (Beinlich et al., 2018). High Mg-content and reactivity, as well as their location in high relief areas near ocean margins make chemical and physical weathering of mafic and ultramafic rocks an important contributor to Mg-fluxes from the continents (e.g. Dessert et al., 2003; Suchet et al., 2003; Ulven et al., 2017). However, the difference in the Mg isotope composition of bulk silicate Earth ($\delta^{26}Mg$ = -0.23 ‰) and that of the continental runoff ($\delta^{26}Mg$ = -1.09 ‰) indicates significant fractionation that can be attributed to the different dissolution rates of isotopically distinct Mg-bearing minerals and to formation of solid weathering product phases, such as clay minerals (Hin et al., 2017; Lai et al., 2015; Tipper et al., 2006a, b; 2010; Teng et al., 2010b). Mg isotope fractionation during formation of Mg-bearing clay minerals is also important for quantification of Mg fluxes into the oceanic clay reservoir, which has been linked to Mg/Ca variations in seawater (Dunlea et al., 2017; Higgins and Schrag, 2015). Furthermore, the formation of secondary silicates and Mg-carbonates during weathering of ultramafic rocks results in distinct Mg-isotope signatures which allow for constraining formation conditions of Mg-carbonate deposits and tracing of Mg during natural sequestration of CO_2 in mafic and ultramafic-derived Mg-carbonates (e.g. Garcia del Real et al., 2016; Oelkers et al., 2019; Oskierski et al., 2013a; Turvey et al., 2018; Wilson et al., 2009; 2014).

Here, for the first time, we present Mg isotope signatures, chemical and mineralogical composition of weathering products from serpentinised peridotite to assess the evolution of Mg isotopes during low temperature continental alteration of ultramafic rocks. In particular, we identify formation of secondary clay minerals as the factor controlling Mg isotope fractionation during weathering of ultramafic rock in the investigated outcrops and show that extreme enrichment of ^{24}Mg in low temperature ultramafic rock-hosted magnesite requires multiple Mg isotope fractionation steps.

2. Sampling locations and geological context

Samples were collected from the Great Serpentinite Belt (GSB), a dismembered, Early Cambrian ophiolite sequence located in northern New South Wales, Australia. U-Pb dating of plagiogranites, considered to be late stage differentiates of the magma from which the ophiolite formed, yield Early Cambrian ages for the crystallisation of the ophiolite (Aitchison et al., 1988; Aitchison and Ireland, 1995). Tectonic or diapiric emplacement of the GSB has been constrained by its emplacement into the Sakmarian Kensington Formation (Vickery et al., 2010) and by its thermal alteration during the intrusion of the Early Permian Bundarra Plutonic Suite, dated at 267.2 ± 1.4 Ma (Cawood et al., 2011). Serpentinite detritus in adjacent Early Permian sandstones and Late Carboniferous to Early Permian nephrite reaction zones in serpentinite indicate that serpentinization occurred before or during the emplacement of the GSB into higher crustal levels (Cross, 1983; Ashley and Brownlow, 1993 and sources therein). The predominance of antigorite at Attunga is likely related to contact metamorphism during the intrusion of the Inlet Monzonite and Attunga Creek Monzogranite in the Early Triassic (Ashley and Brownlow, 1993; Oskierski, 2013). K-Ar dating of fuchsite in silica-carbonate rock yields Early Triassic ages of 243 ± 2 Ma and 251 ± 2 Ma, demonstrating that silica-carbonate alteration occurred after serpentinisation (Ashley and Brownlow, 1993). The radiocarbon content of the nodular magnesite at the study site further suggests that it has formed during Quaternary weathering (Oskierski et al., 2013b). The GSB is exposed along the Peel-Manning Fault (Fig. A1) due to major phases of uplift during the Permian Tablelands and Hunter-Bowen phase of the Gondwanide Orogeny, which are thought to have continued at least until Neogene times (Van der Beek et al., 2001; Vickery et al., 2010). Samples of weathered and silicified serpentinite, saprolite, soil and magnesite were taken from the Attunga magnesite deposit (AMD), located at the south-western tip of a serpentinite ridge (Fig. A1). In outcrop, the upper ~3 m below the pre-mining surface contain pale grey to brown weathered serpentinite (Fig. 1a).

Fig. 1. Field context of investigated samples. **a** Pit wall at the Attunga magnesite deposit showing a thin soil horizon overlying pale to brown weathered serpentinite at the top and magnesite nodules within moderately weathered serpentinite. **b** Saprolite developed above the Attunga magnesite deposit **c** Nodular magnesite displacing weathered serpentinite at the Attunga magnesite deposit. Top scale shows inches and bottom scale cm. **d** White sub-parallel veins cutting boulders of silica-carbonate rocks at the Piedmont magnesite deposit.

The weathered serpentinite grades upwards into an orange-brown, 0.5 m to 2 m thick saprolite horizon that is covered by a thin (5-10 cm) layer of organic-rich soil (Fig. 1b). Weathering of serpentinised harzburgite at Attunga resulted in the formation of cryptocrystalline magnesite veins and nodules (Fig. 1c; Oskierski et al., 2013b). The irregular shape of veins and presence of cauliflower nodules and efflorescence on mining cliff faces point to magnesite formation at low, near-ambient temperature (Oskierski et al., 2013a), consistent with the clumped isotope composition of similar cauliflower magnesite elsewhere (Garcia del Real et al., 2016; Quesnel et al., 2016). Stable O and C isotope and radiocarbon analyses indicate magnesite ages younger than 50 ka and its formation

due to weathering of the serpentinised harzburgite (Oskierski et al., 2013b). Some field observations, such as meter-wide magnesite veins with angular fragments of host rock, imply the prior existence of a silica-carbonate alteration zone at Attunga, which may have been eroded during uplift of the ridge hosting the magnesite (Oskierski et al., 2013b). Due to the extremely slow rates of magnesite formation at ambient temperatures (Hänchen et al., 2007; Königsberger et al., 1999) it has been suggested that low temperature magnesite forms indirectly via a hydrated precursor such as hydromagnesite (Andrews et al., 2018; Gautier et al., 2014; Kralik et al., 1989; Oelkers et al., 2018), which transforms into magnesite over timespans of hundreds of years (Zhang et al., 2000). Cauliflower textures (Fig. 1c) and micro-porosity (Fig. A2) in magnesite nodules at Attunga can thus be interpreted as resulting from volume loss during dehydration (Kralik et al., 1989; Oskierski, 2013). However, recent studies have shown that magnesite can also form directly from low temperature fluids at rates of 10^{-17} to 10^{-16} mol/cm^2/s (Power et al., 2017; 2019) and thus both direct precipitation and indirect formation via a hydrated precursor have to be considered for low temperature magnesite at the study site (Oskierski et al., 2013b). Similar nodular magnesite was also sampled from serpentinised harzburgite pit walls of the Woodsreef Asbestos Mine (WAM). Serpentinite from the Abras Serpentine Quarry (ASQ) is slightly weathered but lacks evidence of carbonation or silicification (Fig. A1).

Samples of weathered serpentinite and nodular, low temperature magnesite are complemented by carbonate samples from higher temperature hydrothermally silica-carbonate altered serpentinite. This alteration is related to the infiltration of hypogene, CO_2-rich fluids between 200 °C and 300 °C in the Early Triassic, which convert serpentinite into quartz, magnesite and/or dolomite (Ashley, 1997). Silica-carbonate alteration zones occur as extensive, irregular lenses mostly along the western margin of the Peel-Manning Fault, e.g. at Hanging Rock (HR) or Trevena Mine (TM) and are characterised by Fe staining and higher Fe-concentrations in coarse grained magnesite (Brownlow and Ashley, 1991; Ashley, 1997).

The Piedmont magnesite deposit (PMD; Fig. 1d) formed by hydrothermal overprinting of a pre-existing silica-carbonate alteration zone at about 200 °C (Ashley, 1995). The microcrystalline,

hydrothermal magnesite at Piedmont occurs in sub-parallel sets of straight veins and is characterised by lower Fe concentrations and smaller grainsize compared to the silica-carbonate host rock (Brownlow and Ashley, 1991; Ashley, 1995). Several generations of brecciation and veining have been documented at Piedmont, including microcrystalline magnesite and colloform quartz-magnesite veins, suggesting the shallow manifestation of a hydrothermal system (Brownlow and Ashley, 1991). Origin, sample type, textural context and mineralogy of the investigated samples are summarised in Table A1.

3. Analytical methods

3.1. Sample preparation and characterisation

Bulk samples were ground in an agate swing mill and smaller samples from select sites and veins were extracted from hand specimen with a diamond coated dental drill. The mineralogy of bulk samples and purity of separates was confirmed by X-ray diffractometry (XRD) using a GBC Enhanced Multi-Materials Analyser at Murdoch University and a PANalytical Empyrean XRD at the Centre for Microscopy, Characterisation and Analysis (CMCA), The University of Western Australia. To constrain clay mineralogy, bulk soil and saprolite powders were suspended in an excess (6-7 drops) of ethanol to allow settling of clay minerals onto the substrate. The oriented powders were then heated to 400 °C and 550 °C for one hour and kept in a desiccator until analysis. The major element composition of bulk samples was determined by X-ray fluorescence (XRF) at Bureau Veritas Australia (Perth), following the procedure described in Oskierski et al. (2013a). The chemical compositions of bulk rock samples and reference materials are listed in Tables A2 and A3, respectively.

3.2. Mg isotope analyses

The magnesium isotopic composition of the samples was determined following the protocol described in Mavromatis et al. (2014a). Bulk samples and separates were digested in concentrated HNO_3 or HF-

HNO_3 mixtures, evaporated to dryness and re-diluted in 1 M HNO_3. About 15 μg of Mg was placed in 10 ml Bio-Rad Poly-prep columns for Mg separation. According to ICP-MS (i.e. Agilent 7500ce) analyses of the eluents, Mg-recovery was better than 99% and the cation/Mg ratio (e.g. Al, Ca, Fe, K, Mn, Na, Ni, Ti) in all samples was < 0.001. Magnesium isotopic compositions were measured using a Thermo-Finnigan 'Neptune' Multi Collector ICP-MS at Géosciences Environnement Toulouse (GET), France using a standard sample induction system (SIS) attached to a PFA Teflon nebuliser. Solutions were ~0.3 M HNO_3 with Mg-concentrations typically ~600 ppb. Measurements of ^{24}Mg, ^{25}Mg, and ^{26}Mg were made in low resolution mode typically providing intensities of ~10-12 V for ^{24}Mg and total procedural blanks generally having a negligible contribution of < 2 mV. Sample-standard bracketing was used to correct instrumental mass fractionation effects and all data are presented as $\delta^x Mg$ with respect to DSM-3 reference material ($\delta^x Mg = ({}^xMg/{}^xMg)_{sample}/({}^xMg/{}^xMg)_{DSM3}-1) \times 1000$), where x refers to the Mg mass of interest. All samples were run in triplicate with the mean values presented in Table 1.

Table 1
Magnesium isotope composition and MgO/SiO2* of analysed samples

Sample ID	Location	Sample type	MgO/SiO_2*[b]	$\delta^{26}Mg_{DSM-3}$ (‰)	2σ	$\delta^{25}Mg_{DSM-3}$ (‰)	2σ	n
Altered/weathered serpentinite								
AT1-1	ASQ	Serpentinite	0.09	-0.04	0.05	-0.01	0.00	3
AT35	AMD	Weathered serpentinite	0.41	0.08	0.02	0.05	0.01	3
AT100/4	AMD	Weathered silicified serpentinite	0.90	0.02	0.05	0.02	0.06	3
AT100/3	AMD	Weathered silicified serpentinite	0.89	0.09	0.01	0.06	0.02	3
AT100/3 (repeat)	AMD	Weathered serpentinite	0.89	0.10	0.02	0.05	0.03	3
AT30-1	AMD	Saprolite	0.22	0.01	0.01	0.00	0.03	3
AT106	AMD	Saprolite	0.56	0.37	0.03	0.18	0.05	3
AT104	AMD	Saprolite	0.52	0.20	0.06	0.09	0.04	3
AT105	AMD	Soil	0.48	0.13	0.09	0.07	0.02	3
Nodular magnesite[a]								
ATMNDC_185	AMD	Magnesite	*ND*	-2.55	0.03	-1.33	0.04	3
ATMNDC_185 (repeat)	AMD	Magnesite	*ND*	-2.57	0.05	-1.34	0.03	3
ATMNDC1_3	AMD	Magnesite	*ND*	-2.67	0.06	-1.38	0.06	3
AT37-1-1DM	AMD	Magnesite	*ND*	-2.55	0.09	-1.31	0.04	3
WOMP-M1	WAM	Magnesite	*ND*	-3.26	0.10	-1.67	0.01	3

Hydrothermal carbonate[a]/carbonated serpentinite								
TM-D3	TM	Silica carbonate	*ND*	-0.35	0.04	-0.18	0.02	3
HR-D1	HR	Dolomite	*ND*	-0.62	0.09	-0.33	0.04	3
B2-1DB	PMD	Magnesite	*ND*	-0.69	0.10	-0.37	0.04	3
Standards								
JDo-1		Dolomite	*ND*	-2.43	0.04	-1.23	0.04	6
BE-N		Basalt	*ND*	-0.27	0.05	-0.14	0.03	3
CAM1		monoelemental solution	*ND*	-2.62	0.06	-1.33	0.05	15
OUMg		monoelemental solution	*ND*	-2.82	0.07	-1.42	0.05	15

ND = not determined
n = no. of measurements

[a] Distinction between nodular and hydrothermal carbonate based on Ashley (1995, 1997), Oskierski et al. (2013a, 2013b)

[b] MgO/SiO_2* = $(MgO/SiO_2)_{fractionation\ array}$ - $(MgO/SiO_2)_{sample}$ = deviation from the terrestrial fractionation array as proxy for degree of weathering

The reproducibility of replicate δ^{26}Mg analyses of Mg reference standards was typically better than 0.07 ‰ (2 σ). This precision is similar to that reported earlier from our laboratory (Pearce et al., 2012; Beinlich et al., 2014; 2018; Mavromatis et al., 2012, 2013, 2014a,b, 2016; Shirokova et al., 2013; Schott et al., 2016). Moreover, standards processed identically to samples, produced isotopic compositions similar to those reported elsewhere (Table 1; see values in Pearce et al., 2012; Shalev et al., 2018; Wombacher et al., 2009 for comparison).

3.3. Carbon and oxygen isotope analyses

Stable carbon and oxygen isotope ratios of carbonate samples were determined using a GV2003 Continuous-Flow Isotope Ratio Mass Spectrometer (IRMS) at the University of Newcastle and a Gasbench connected to a Delta V XL IRMS at the University of Western Australia (UWA). Carbonate samples were reacted with phosphoric acid overnight at 72 °C or 80 °C. In the absence of a suitable magnesite reference material results were normalised to in-house calcite standards that are calibrated using commercially available reference materials L-SVEC (for C only), NBS18 and NBS19 (Skrzypek, 2013). Certified reference materials were run as unknowns to validate results. Correction factors for oxygen isotope fractionation during reaction of magnesite, dolomite (and calcite) with phosphoric acid were taken from Das Sharma et al. (2002). Reproducibility, defined as the 1σ

standard deviation of repeat measurements of in-house standards, is < 0.1 ‰ for both $\delta^{13}C$ and $\delta^{18}O$ (Table 2).

Table 2
Carbon and oxygen isotope signatures and formation temperatures of studied carbonates

Sample ID	Location	Sample type	$\delta^{13}C_{VPDB}$ (‰)	1σ	$\delta^{18}O_{VSMOW}$ (‰)	1σ	Formation temp. (°C)
Nodular magnesite							
ATMNDC_185	AMD	Magnesite	-12.3[a]	0.1	28.1[a]	0.1	41[c]
ATMNDC1_3	AMD	Magnesite	-11.7[a]	0.1	28.7[a]	0.1	38[c]
AT37-1-1DM	AMD	Magnesite	-12.5[a]	0.1	29.0[a]	0.1	37[c]
WOMP-M1	WAM	Magnesite	*ND*	*ND*	*ND*	*ND*	38[d]
Hydrothermal carbonate							
TM-D3	TM	Dolomite	-4.8	0.1	14.8[b]	0.1	243[e]
HR-D1	HR	Dolomite	-4.3	0.2	15.3[b]	0.2	216[e]
B2-1DB	PMD	Magnesite	5.6	0.2	27.9	0.2	200[f], 99[g]

ND = not determined

[a] Data from Oskierski et al. (2013b)
[b] Corrected for oxygen isotope fractionation during reaction of dolomite with phosphoric acid (Das Sharma et al., 2002)
[c] Oxygen isotope thermometry based on $\delta^{18}O$ of precipitation (Liu et al., 2010) and 1000 $\ln\alpha_{mgs\text{-}H2O}$ from Aharon (1988)
[d] Based on oxygen isotope thermometry of spatially associated sample WR-102 (Oskierski et al., 2013c)
[e] Fluid inclusion homogenisation temperatures in associated quartz from Ashley 1997 (range HR-D1 156-261 °C; TM-D3 220-271 °C)
[f] Fluid inclusion homogenisation temperatures in associated quartz from Ashley 1995 (range 170 to 230 °C)
[g] Oxygen isotope thermometry based on $\delta^{18}O$ of magmatic/metamorphic fluid (Ashley, 1995) and 1000 $\ln\alpha_{mgs\text{-}H2O}$ from Aharon (1988)

3.4. Geochemical modelling

Geochemical modelling of aqueous Mg speciation was carried out using PHREEQC (Parkhurst and Appelo, 2013) with the wateq4f database suitable for freshwater with relatively low total dissolved solid loads such as the studied sample (Oskierski et al., 2016). The database was modified to include the carbonic acid dissociation constants of Stefansson et al., (2013), the formation constants of $MgCO_3$ and $MgHCO_3^-$ determined by Stefansson et al., (2014) and the Mg hydrolysis constant of Palmer and Wesolowski (1997). The distribution of aqueous species was used to estimate the Mg isotopic composition of aqueous Mg^{2+} relative to the bulk fluid, based on the fractionation factors from Schott et al., (2016) at 38 °C, the inferred average formation temperature of nodular magnesite. Further details are presented in table A4.

4. Results

4.1. Mineralogy and bulk chemical composition of serpentinite and alteration products

The least altered serpentinite consists predominantly of serpentine with accessory magnetite, hematite and andradite (Table A1) and the chemical composition is typical of serpentinised harzburgites in the study area (Table A2; Ashley, 1997).

The altered serpentinised harzburgites include silicified and weathered serpentinites, as well as saprolites and soil developed on serpentinite. In the silicified serpentinite, opaline silica occurs as the dominant phase together with minor amounts of antigorite, magnetite and hematite, which is also reflected in SiO_2 concentrations above 66 wt %. Antigorite, identified by the (330) reflection that is absent in XRD patterns of lizardite and chrysotile, is a major phase in most serpentinite weathering products at AMD and secondary clay becomes dominant in highly weathered saprolites and soil developed from the serpentinite. Figure 2 illustrates the collapse of the ~ 15 Å peak of the clay mineral to ~ 10 Å upon heating to 400 and 550 °C. This indicates that the clay mineral is interstratified illite-vermiculite or illite-montmorillonite and confirms that chlorite/clinochlore is absent from the weathering profile (Poppe et al., 2001).

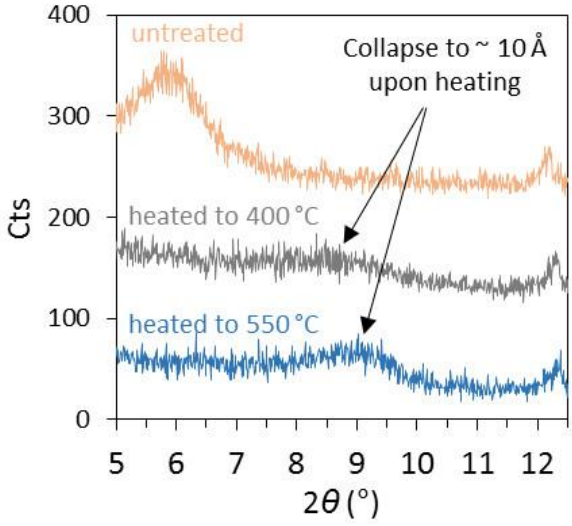

Fig. 2. XRD patterns of saprolite sample AT106. The ~15 Å peak of the clay mineral collapses to ~ 10 Å upon heating to 400 and 550 °C.

Chemical compositions vary from typical serpentinite to highly weathered, MgO-depleted saprolite, with MgO concentration as low as 6.9 wt. % (Table A2). We calculate the deviation of the sample compositions from the terrestrial fractionation array in the Al_2O_3/SiO_2 - MgO/SiO_2 space as $(MgO/SiO_2)_{fractionation\ array}$ - $(MgO/SiO_2)_{sample}$ = MgO/SiO_2* (Snow and Dick, 1995; Liu et al., 2017). The degree of weathering, represented by MgO/SiO_2*, is low for relatively unaltered serpentinite (0.1), increases for weathered serpentinite, saprolite and soil (0.2 to 0.6) and is high for silicified serpentinites (0.4-0.9; Table 1; Fig. 3).

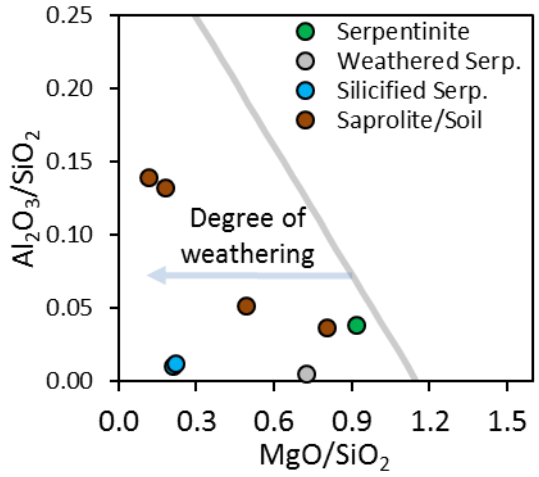

Fig. 3. Cross-plot of Al_2O_3/SiO_2 and MgO/SiO_2 ratios showing degree of weathering as the deviation from the terrestrial geochemical fractionation array of peridotites (grey, solid line with Al_2O_3/SiO_2 = -3.406 MgO/SiO_2 + 1.148; Snow and Dick, 1995).

4.2. Mineralogy and bulk chemical composition of carbonate altered samples

Nodular, ultramafic-hosted carbonates are magnesite (Table A1) with low Fe-content (Table A2) compared to typical hydrothermal magnesite and dolomite in silica-carbonate rocks from the GSB (Ashley, 1995; 1997). The hydrothermal carbonates comprise dolomite in silica-carbonate rock and magnesite from veins in silica-carbonate rock (Ashley, 1997). Bulk silica-carbonate altered ultramafic rock (TM-D3) is composed of dolomite, quartz and clinochlore. If present, contaminants in the carbonate samples are devoid of Mg (as e.g. quartz) or are present in low quantity (< 5 wt. %), as e.g. pyroaurite and serpentine.

4.3. Mg isotope signatures

Linear regression through all samples in a three isotope plot of δ^{26}Mg against δ^{25}Mg defines a slope of -0.515, consistent with mass dependent fractionation (Fig. A3; Young and Galy, 2004). Figure 4 shows the Mg isotope composition of the studied samples relative to other ultramafic rocks and associated alteration products from the literature.

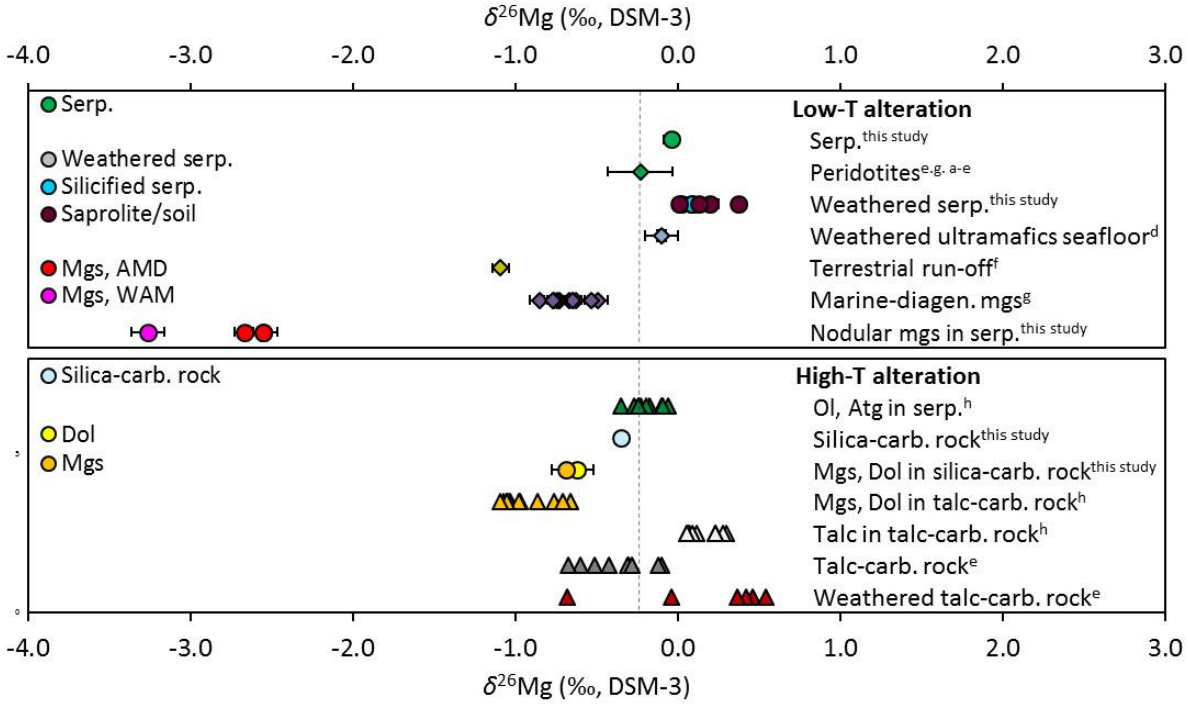

Fig. 4. Mg isotopic fingerprint of ultramafic rocks and associated alteration products. [a]Teng et al., (2010b); [b]Lai et al., 2015; [c]Hin et al., (2017); [d]Liu et al., (2017); [e]Beinlich et al., (2018); [f]Tipper et al., (2006a); [g]Dong et al., (2016); [h]Beinlich et al., (2014). δ^{26}Mg of bulk silicate Earth is shown as dashed line. Please note that signatures of weathered and silicified serpentinites are covered by those of saprolite/soil. Serp. = Serpentinite, Mgs = magnesite, Ol = olivine, Atg = antigorite, Dol = dolomite.

The least weathered serpentinite sample has a δ^{26}Mg of -0.04 ‰, which is higher than the average of pristine magmatic rocks (δ^{26}Mg of -0.23 ‰; Hin et al., 2017; Lai et al., 2015). Weathered bulk rock samples have elevated δ^{26}Mg values between 0.01 ‰ and 0.37 ‰ (Table 1; Fig. 4). The Mg isotope composition of magnesite separates varies between -3.26 ‰ and -0.69 ‰, which is comparable to the known range of dolomite compositions (-2.49 ‰ < $\delta^{26}Mg_{dol}$ < -0.45 ‰, e.g. Geske et al., 2015a). δ^{26}Mg values of ultramafic rock-hosted nodular and vein magnesite (-3.26 ‰ < δ^{26}Mg <

-2.55 ‰) fall within a distinct range compared to hydrothermal magnesite and dolomite (δ^{26}Mg = -0.69 ‰ and -0.62 ‰). Geochemical modelling of aqueous Mg speciation in a weathering fluid from one of the study sites shows that 70.1 % of Mg occur as Mg^{2+}, 24.4 % as $MgCO_3°$, 5.3 % as $MgHCO_3^+$ and 0.2 % as $MgOH^+$, whereas the proportions of other aqueous complexes are negligible (Table A4). If Mg in the weathering fluid is predominantly derived from the weathering of pristine ultramafic rock ($\delta^{26}Mg_{fluid}$ = -0.28 ‰, as calculated in section 5.4) inter-species Mg isotope fractionation leads to enrichment of ^{26}Mg in $MgCO_3°$ ($\delta^{26}Mg_{MgCO3°}$ = 3.2 ‰), $MgHCO_3$ ($\delta^{26}Mg_{MgHCO3+}$ = 2.1 ‰) and $MgOH^+$ ($\delta^{26}Mg_{MgOH+}$ = 0.3), leaving Mg^{2+} enriched in ^{24}Mg ($\delta^{26}Mg_{Mg2+}$ = -1.7 ‰).

4.4. Carbonate stable O and C isotope signatures and formation temperatures

The δ^{13}C and δ^{18}O of the studied carbonate samples range from -12.5 ‰ to 5.6 ‰ and from 14.8 ‰ to 29.0 ‰, respectively (Table 2; Fig. 5).

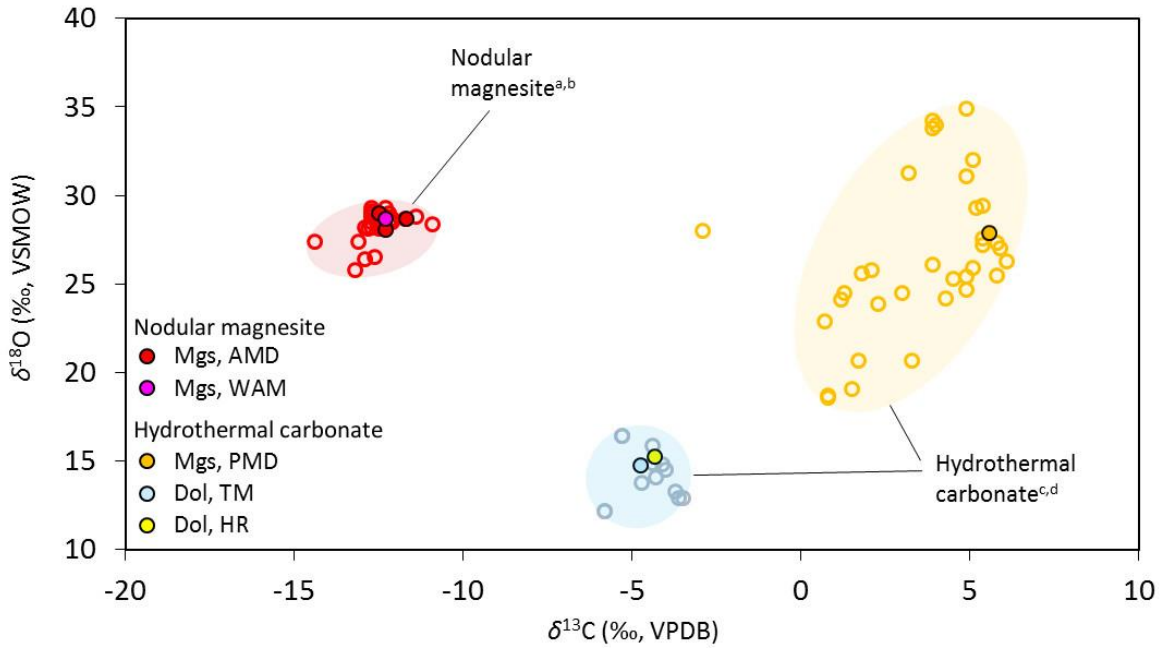

Fig. 5. Stable carbon and oxygen isotope signatures of ultramafic-derived carbonates. Reference values for the same deposits are shown as open circles. [a]Oskierski et al., 2013a; [b]Oskierski et al., 2013b; [c]Ashley, 1997; [d]Ashley, 1995.

Carbon isotope ratios are low for nodular, ultramafic rock-hosted magnesite from the AMD (δ^{13}C of -12.5 ‰ to -11.7 ‰) and the WAM (δ^{13}C of -12.3 ‰ for spatially associated sample WR-

102, see Oskierski et al., 2013c). The low $\delta^{13}C$ either represents kinetic isotope fractionation during uptake of CO_2 into water (Andrews et al., 2017; Wilson et al., 2010) or C3 plants as the dominant source of carbon, suggesting a formation of magnesite nodules from meteoric water at low temperatures (Oskierski et al., 2013c). We estimate formation temperatures between 37 ºC and 41 ºC (average 38 ºC, n = 4) for nodular magnesite based on oxygen isotope thermometry using fractionation factors from Aharon (1988). In the absence of paleo-fluid samples we assume the average oxygen isotope composition of recent meteoric water ($\delta^{18}O$ = -4.91 ‰, Liu et al., 2010b) to be representative of the weathering fluid at the time of magnesite formation. The assumed water composition and uncertainty in the fractionation factor result in significant uncertainty in the estimated temperatures, i.e. a 1 ‰ change in $\ln\alpha_{mgs\text{-}H2O}$ results in a ~5 °C change of the estimated temperature. However, textures and ^{14}C content confirm that nodular and vein magnesite at AMD has formed from meteoric water at near ambient temperatures (Oskierski et al., 2013a). This is further corroborated by $\delta^{18}O$ values above 28.0 ‰ (Table 2, Fig. 5), which suggest (i) magnesite precipitation from meteoric water; (ii) large oxygen isotope fractionation during precipitation at low temperature; and (iii) magnesite precipitation driven by fluid evaporation (Aharon, 1988; Beinlich and Austrheim, 2012; Oskierski et al., 2013a, b; 2016). The estimated temperatures are further in agreement with temperatures determined by clumped isotope thermometry on texturally similar cryptocrystalline magnesite elsewhere (Garcia del Real et al., 2016; Quesnel et al., 2016).

Hydrothermal dolomite in silica carbonate rock has $\delta^{13}C$ values of -4.8 ‰ and -4.3 ‰ and $\delta^{18}O$ of 14.8 ‰ and 15.3 ‰, which are typical for silica carbonate rock in the study area and significantly higher and lower than those of the nodular magnesite, respectively (Fig. 5). Formation temperatures of 243 ºC and 216 ºC have been estimated for Mg-carbonates in silica carbonate rock in the study area based on fluid inclusion microthermometry of associated quartz, that are consistent with the low $\delta^{18}O$ of the carbonates (Table 2; Ashley, 1997). Together, these values have been interpreted to reflect a homogenised magmatic carbon source (average $\delta^{13}C_{CO2\text{-}source}$ ~ -5.4 ‰) and magmatic or metamorphic fluids (average $\delta^{18}O_{fluid}$ ~ 6.0 ‰; Ashley, 1997) based on fractionation factors from Aharon (1988).

Magnesite from Piedmont is characterised by high $\delta^{13}C$ of 5.6 ‰ and high $\delta^{18}O$ of 27.9 ‰, with fluid inclusions in intergrown quartz indicating formation temperatures of about 200 ºC (Ashley, 1995). This unusual signature was previously interpreted to result from the interaction of metamorphic fluids with evaporitic carbonates, isotopic equilibration with CH_4 or CO_2 degassing from fluids (average $\delta^{13}C_{CO2\text{-}source}$ ~ 3.6 ‰; average $\delta^{18}O_{fluid}$ ~ 15.5 ‰; Ashley, 1995). The high $\delta^{18}O$ compared to the silica carbonate host rock may also point to a cooling of fluids (Ashley, 1995; Brownlow and Ashley, 1991) and oxygen isotope thermometry yields a formation temperature of 99 ºC for a magmatic/metamorphic ($\delta^{18}O_{fluid}$ ~ 6.0 ‰) fluid source. However, sub-parallel veins and breccia textures indicate that magnesite at Piedmont formed from hydrothermal fluids and not from dissolution reprecipitation of the pre-exisiting silica-carbonate rock. Both the textures of silica-carbonate rock (HR, TM) and hydrothermal magnesite from Piedmont (PMD) are clearly distinct from the low-temperature, nodular magnesite occurrences (Ashley, 1995; 1997) and there is no clear relationship between $\delta^{18}O$ and $\delta^{26}Mg$ of magnesite.

5. Discussion

5.1. Ultramafic rock weathering

The alteration products of partly serpentinised harzburgite have lower MgO concentrations and MgO/SiO_2 than the serpentinite precursor (Table A2; Ashley, 1995; Oskierski et al., 2013b). This reflects the release of Mg into weathering fluids (Beinlich et al., 2010; Oskierski et al., 2016) and the residual enrichment of SiO_2 during early stages of weathering, whereas progressive weathering and laterisation enrich Al_2O_3 and Fe_2O_3 relative to SiO_2 (Beinlich et al., 2018; Oskierski et al., 2013b; Snow and Dick, 1995). This chemical change in the bulk rock is also reflected in the secondary minerals forming during weathering (Fig. A4), i.e. clay minerals replacing serpentine contain less MgO but are enriched in the least mobile components, Al_2O_3 and Fe_2O_3, relative to the serpentinite precursor (Caillaud et al., 2006). The increasing deviation of weathered sample compositions from the

terrestrial geochemical fractionation array illustrates the transition from relatively fresh serpentinite, over weathered serpentinite, to soil and saprolite (Fig. 3).

5.2. Mg-isotope fractionation during ultramafic rock weathering

The δ^{26}Mg value of the least altered serpentinite from the study area is slightly higher than the composition of pristine mafic and ultramafic rocks (Beinlich et al., 2018; Hin et al., 2017; Lai et al., 2015) but in agreement with antigorite separates from Norwegian ophiolite sequences (Beinlich et al., 2014). Decreasing MgO concentrations and increasing degree of weathering, as expressed by the proxy MgO/SiO_2* (Fig. 3; Liu et al., 2017; Snow and Dick, 1995), are correlated with increasing δ^{26}Mg of the serpentine weathering products (Fig. 6a, b).

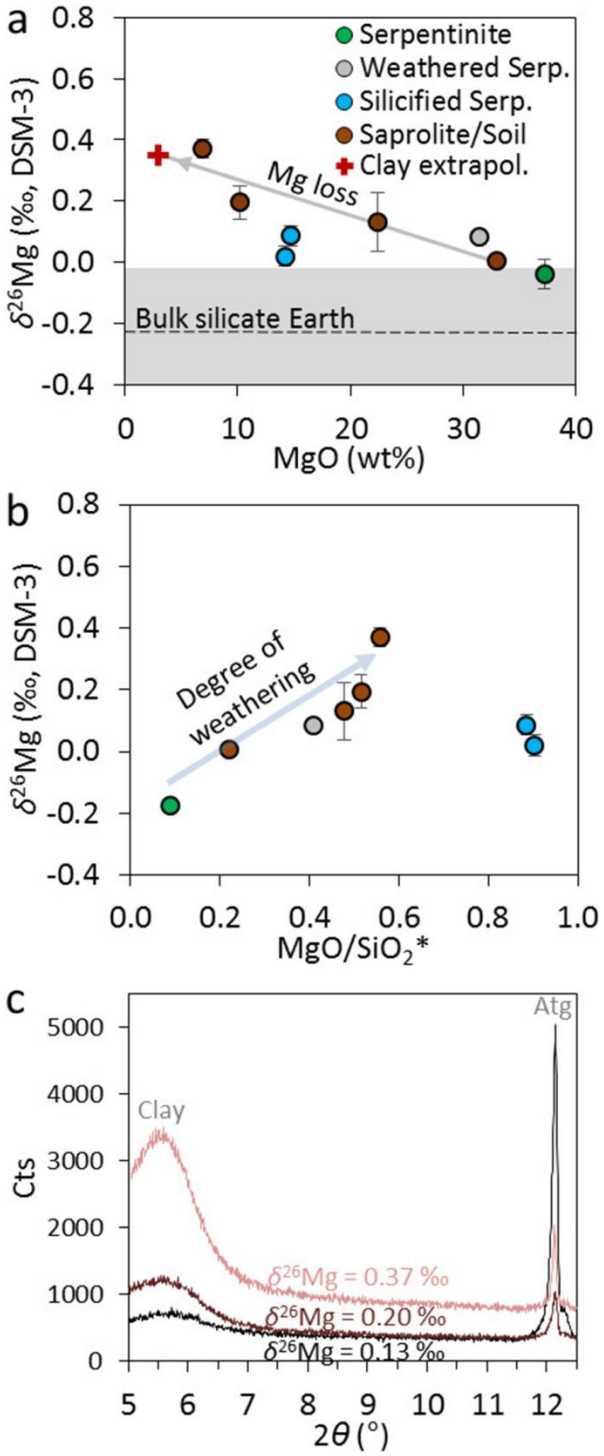

Fig. 6. Mg isotope systematics of ultramafic rock weathering products. **a** Negative correlation between δ^{26}Mg and MgO-content of serpentinite and weathering products. The grey area represents Mg isotopic compositions of mafic and ultramafic rocks and the dashed line bulk silicate Earth (Hin et al., 2017; Lai et al., 2015). The red cross indicates the δ^{26}Mg for linear extrapolation of the soil/saprolite samples to a MgO concentration of 3%. The equation of the linear fit through the saprolite/soil samples is δ^{26}Mg = -0.0118 MgO (wt %) + 0.3907. **b** Positive correlation between δ^{26}Mg and MgO/SiO_2*, a

proxy representing the degree of weathering (see Fig. 3). **c** XRD patterns of saprolite/soil samples from AMD showing mineralogical control on δ^{26}Mg during ultramafic rock weathering.

This indicates preferential retention of ^{26}Mg in the saprolite as has been observed during marine weathering of abyssal peridotites by Liu et al., (2017). Both the increase in δ^{26}Mg and degree of weathering corresponds to increasing clay mineral content in the soil and saprolite (Fig. 6c), suggesting a mineralogical control of the Mg-isotope fractionation during terrestrial weathering of ultramafic rocks.

5.3. Factors controlling Mg-isotope fractionation during ultramafic rock weathering

Despite the potential presence of a silica-carbonate precursor in higher, now eroded stratigraphic levels at the study site (Oskierski et al., 2013b), we can exclude differential weathering as the reason for enrichment of ^{26}Mg in the saprolite based on the absence of ^{26}Mg-enriched talc and/or chlorite from the weathering profile (Beinlich et al., 2014; 2018). Low organic carbon levels and high content of phytotoxic metals (Ni, Cr) in the saprolite (Oskierski et al., 2013b), render control of Mg isotope fractionation by soil exchange processes (Opfergelt et al., 2012; 2014; Pokharel et al., 2017), unlikely and the high Mg content of the soil and saprolite (6.9 to 33.0 % MgO) relative to typical dust in Eastern Australia (0.22 % MgO; Dickson and Scott, 1998) suggests that Aeolian inputs have a negligible influence on δ^{26}Mg of the saprolites.

The observed concurring changes in chemical composition, mineralogy and isotopic composition are consistent with previous studies documenting the retention of ^{26}Mg by secondary (silicate) phases during continental (Beinlich et al., 2018; Huang et al., 2012; Lara et al., 2017; Liu et al., 2014; Teng et al., 2010a) and marine weathering (Liu et al., 2017). However, variable δ^{26}Mg and preferential retention of ^{24}Mg in natural weathering residues (Huang et al., 2012; Opfergelt et al., 2014; Pogge von Strandmann et al., 2008; 2012) and in experimentally precipitated secondary silicates (Ryu et al., 2016; Wimpenny et al., 2010) have been documented. The direction and magnitude of Mg isotope fractionation during weathering thus depend on the exact weathering process (Teng, 2017) and, in particular, on primary and secondary phase mineralogy (Huang et al.,

2012; Li et al. 2014), weathering intensity (Liu et al., 2014) and the proportions of isotopically distinct structurally-bound and labile Mg (Wimpenny et al., 2014). Fast, concurrent precipitation of carbonates may deplete ^{24}Mg in weathering fluids and thus in the exchangeable Mg fraction of the weathering residue, which commonly reflects the Mg isotopic composition of associated fluids (Huang et al., 2012; Lara et al., 2017; Liu et al., 2014; Wimpenny et al., 2014). However, clay minerals at our study site are Mg-rich illite-vermiculite or illite-montmorillonite (Fig. 2) and structurally bound Mg thus dominates the Mg budget of the weathering products. This confirms that clay formation controls Mg isotope fractionation during continental weathering, as inferred by Liu et al., (2017) for marine weathering of peridotite. Extrapolation of the relationship between $\delta^{26}Mg$ and MgO content of the saprolite shows that a saprolite containing only clay, e.g. montmorillonite or illite with 3 % MgO, will have a $\delta^{26}Mg$ of ~ 0.35 ‰ (Fig. 6a). The apparent Mg isotope fractionation between fluid and clay at ambient temperature is ~ 0.4 ‰ to ~ 0.6 ‰, estimated as $\Delta^{26}Mg_{clay\text{-}fluid} = \delta^{26}Mg_{clay} - \delta^{26}Mg_{fluid}$ with $\delta^{26}Mg_{fluid}$ approximated by the composition of either pristine peridotite ($\delta^{26}Mg$ = -0.23 ‰) or the least weathered serpentinite from the study site ($\delta^{26}Mg_{serpenttite}$ = -0.04 ‰). This value is consistent with the range of Mg isotope fractionation ($\Delta^{26}Mg_{peridotite\text{-}fluid}$ ~ 0.2 ‰ to 1.0 ‰) derived from Rayleigh modelling of the weathering of peridotite on the seafloor (Liu et al., 2017). It is noteworthy that high temperature experiments between 90 and 250 °C result in similar Mg-isotope fractionation between TOT clay (T = tetrahedral and O = octahedral layer) and fluid ($\Delta^{26}Mg_{clay\text{-}fluid}$ of 0.54 ‰; Ryu et al., 2016). However, experimental studies using brucite as an analogue for clays found that Mg-isotope fractionation between brucite and fluid decreases with temperature, i.e. from -0.3 ‰ at 7 °C to 0.5 ‰ at 80 °C (Li et al., 2014; Wimpenny et al., 2014), whereas first principle calculations predict the opposite trend with positive $\Delta^{26}Mg_{brucite\text{-}fluid}$ at all temperatures (Wang et al., 2019).

5.4. Constraints on Mg isotope signatures of weathering fluids

The fractionation of Mg isotopes during partial melting and magmatic differentiation is small (e.g. Dauphas et al., 2010; Liu et al., 2010a; Teng et al., 2010b) and similar Mg isotope signatures of olivine, pyroxene and serpentine separates indicate that serpentinisation does not alter the Mg isotope

signatures of ultramafic rocks (Beinlich et al., 2014; Liu et al., 2017). Therefore, we use the isotope composition of pristine peridotite (δ^{26}Mg = -0.23 ‰; Hin et al., 2016; Lai et al., 2017) to represent the isotopic composition of Mg in the serpentinite prior to weathering, rather than referring to the least altered sample from the study area, for which a slightly elevated δ^{26}Mg (Table 1) may point to incipient weathering.

First-principles calculations suggests that significant equilibrium Mg isotope fractionation occurs between the serpentine mineral lizardite and aqueous Mg^{2+}, as well as magnesite and aqueous Mg^{2+}, respectively (Wang et al., 2019). Mg isotope fractionation between carbonates or silicates and fluid is also observed in experimental dissolution studies but is not commonly ascribed to fractionation during incongruent dissolution but to the reprecipitation of the dissolving mineral in a dynamic exchange equilibrium or to secondary phase formation (e.g. Oelkers et al., 2018; Pearce et al., 2012; Wimpenny et al., 2010). Mass balance calculations confirm that Mg isotopes in serpentinite are distributed into secondary silicate and carbonate phases during talc-carbonate alteration (Beinlich et al., 2014). Along with the absence of Mg isotope fractionation during serpentinization this demonstrates that hydrothermal alteration and serpentinisation occur without inherent Mg isotope fractionation between serpentine and fluids (Beinlich et al., 2014; Liu et al., 2017). Above, we demonstrate that Mg isotope fractionation during weathering of serpentinite is controlled by the retention of ^{26}Mg in secondary clay minerals, implying that ^{24}Mg is preferentially released into weathering fluids. As a first approximation, we use a closed system isotope balance to constrain the isotopic composition of fluids resulting from the decomposition of serpentinite to saprolite at the weathering profile scale:

$$\delta^{26}Mg_{serpentinite} \approx \delta^{26}Mg_{peridotite} = f\,\delta^{26}Mg_{saprolite} + (1\text{-}f)\,\delta^{26}Mg_{fluid} \quad (1)$$

with f referring to the mass fraction of Mg remaining in the saprolite, calculated relative to fresh serpentinite from the GSB (Ashley, 1997). For complete conversion of fresh serpentinite to illite or montmorillonite with ~ 3 wt % MgO (f = 0.08) the isotope balance predicts $\delta^{26}Mg_{fluid}$ of -0.28 ‰, which is close to the isotopic composition of fresh serpentinite used in the calculation (δ^{26}Mg = -0.23

‰). The calculation suggests that the retention of small amounts of heavy Mg in the saprolite has only a small effect on the Mg isotopic composition of the weathering fluids from ultramafic rocks.

Some textural evidence at Attunga suggest that the formation of nodular, low temperature magnesite may have been preceded by hydrothermal alteration of the host-rock to silica-carbonate rock, which has subsequently been eroded (Oskierski et al., 2013b). As magnesite and dolomite dissolve faster during interaction with CO_2-bearing meteoric fluids than secondary silicate phases (Bales and Morgan, 1985; Pokrovsky and Schott, 2000; Pokrovsky et al., 2009; Saldi et al., 2007), weathering of silica-carbonate rock would predominantly release light Mg into weathering fluids. Furthermore, Mg-carbonates are absent from weathered talc-carbonate rock (Beinlich et al., 2018), attesting to complete dissolution of Mg-carbonates during weathering. In line with isotope/mass balance considerations precluding isotope fractionation during complete dissolution and predominant far-from-equilibrium conditions during weathering we assume that there is no significant Mg isotope fractionation during dissolution of Mg-carbonates in silica-carbonate rock. The Mg isotopic composition of fluids from weathering of silica-carbonate rock can thus be represented by a $\delta^{26}Mg_{fluid}$ of ~ -0.66 ‰, which corresponds to the average $\delta^{26}Mg$ of hydrothermal magnesite and dolomite separates from the GSB (Table 1).

5.5. Mg isotope signatures of magnesite formed during ultramafic rock weathering

5.5.1. Mg source

The Mg isotope signature of magnesite generally depends on the isotopic composition of the Mg source (e.g. Tipper et al., 2006a, b), the fluid chemical composition that can strongly affect the Mg isotope composition of aqueous Mg species due to inter-species Mg isotope fractionation (Schott et al., 2016; Mavromatis et al., 2017a, b) and fractionation during precipitation (e.g. Li et al., 2012, 2015; Rustad et al., 2011). The textures, stable C and O isotope compositions and radiocarbon content demonstrate that the studied nodular and vein magnesite formed during ultramafic rock weathering (Table 2; Oskierski et al., 2013b). The Mg isotope signature of bulk fluids thus results from the

interaction of CO_2-bearing meteoric water with the partly serpentinised, isotopically homogeneous host rock and/or a pre-existing silica-carbonate rock. As a first approximation, these fluids can be represented by a $\delta^{26}Mg_{fluid}$ of ~ -0.28 ‰ and ~ -0.66 ‰, reflecting the fluid composition after complete dissolution of fresh peridotite and clay formation and completely dissolving magnesite and/or dolomite in silica-carbonate rock, respectively.

5.5.2. Inter-species Mg-isotope fractionation

Aqueous Mg-speciation and the associated inter-species Mg isotope fractionation, particularly between Mg^{2+}, $MgHCO_3^+$ and $MgCO_3°$, have been shown to influence the Mg isotope signatures of carbonate precipitates (Schott et al., 2016). The analysis of experimental (Mavromatis et al., 2012) and natural samples (Shirokova et al., 2013) indicates that the $\delta^{26}Mg$ value of Mg^{2+} can be 1.3 ‰ to 1.8 ‰ below that of the total dissolved Mg in an alkaline solution at ambient temperatures and pH > 9 due to the preferential enrichment of ^{26}Mg into $MgHCO_3^+$ and $MgCO_3°$ (Schott et al., 2016). Low-temperature, ultramafic rock buffered weathering fluids are alkaline, with pH and DIC ranging from 8.4 to 10.6 and 0.9 to 8.7 mM, respectively (Beinlich and Austrheim, 2012; Oskierski et al., 2016), implying that magnesite precipitating from Mg^{2+} in these fluids is expected to be enriched in ^{24}Mg relative to total dissolved Mg. In weathering fluids from the Woodsreef Asbestos Mine (Oskierski et al., 2016) up to 30 % of aqueous Mg occurs as $MgHCO_3^+$ and $MgCO_3°$, leading to Mg^{2+} that is ~1.4 ‰ lighter than the bulk fluid $\delta^{26}Mg$ due to inter-species fractionation (Oskierski et al., 2016; Schott et al., 2016; see table A4 for details). Considering weathering of pristine ultramafic rock ($\delta^{26}Mg_{fluid}$ of -0.28 ‰) or magnesite and dolomite in silica carbonate rock ($\delta^{26}Mg_{fluid}$ ~ -0.66 ‰) as the dominant source of Mg in weathering fluids, Mg isotope fractionation between aqueous Mg species would lead to aqueous Mg^{2+} in weathering fluids with $\delta^{26}Mg_{Mg^{2+}}$ of ~ -1.7 ‰ and ~ -2.1 ‰, respectively.

5.5.3. Mg isotope fractionation during precipitation

As heavy isotopes are preferentially incorporated into minerals that exhibit shorter/stronger Mg-O bonds compared to that of the hexahydrated aqueous Mg^{2+} ion, Mg bonding in the solid phase is fundamental in controlling the Mg isotope composition of different carbonate minerals (Geske et

al., 2015a; Li et al., 2014, 2015; Mavromatis et al., 2017a; Pinilla et al., 2015; Perez-Fernandez et al., 2017). Formation of low temperature magnesite via a hydrated precursor may thus result in a distinct Mg isotope signature compared to magnesite precipitated directly from low temperature fluids. Hydrated Mg-carbonates precipitated rapidly (Harrison et al., 2017) preferentially incorporate light Mg (Mavromatis et al., 2012; Shirokova et al., 2013; Oelkers et al., 2018) and at room temperature fractionation factors between hydrated Mg-carbonates and fluids range between -1.17 ‰ and -1.43 ‰ for dypingite (Mavromatis et al., 2012) and -0.25 ‰ (Oelkers et al., 2018) or -0.9 ‰ to -1.1 ‰ for hydromagnesite (Shirokova et al., 2013).

Among these hydrated Mg carbonates, hydromagnesite is the most stable under surface conditions (Hänchen et al., 2007; Königsberger et al., 1999; Harrison et al., 2019) and most commonly associated with magnesite deposits (Andrews et al., 2018; Kralik et al., 1989; Power et al., 2014). Furthermore, hydromagnesite forms during recent weathering of peridotite mine tailings at ambient temperatures in the study area, whereas other hydrated Mg-carbonate minerals are absent (Oskierski et al., 2013c; 2016). For simplicity, we thus consider hydromagnesite as the most likely precursor to magnesite. The transformation of hydromagnesite into magnesite can occur either via (thermal) dehydration (Hollingberry and Hull, 2010; Zhang et al., 2000) or dissolution/re-precipitation (Di Lorenzo et al., 2014; Königsberger et al., 1999; Zhang et al., 2000), with the latter inducing an additional Mg-isotope fractionation step with $\Delta^{26}Mg_{hmgs\text{-}fluid}$ ~ -1.0 ‰ (Shirokova et al., 2013) in the formation pathway of low temperature magnesite.

An inverse correlation between precipitation rates and the magnitude of Mg isotope fractionation with the fluid has been observed for calcite precipitation at ambient temperatures (Immenhauser et al., 2010; Mavromatis et al., 2013). Considering that precipitation rates of magnesite and hydromagnesite are ~6 and ~3 orders of magnitude slower than for calcite at 25 °C (Gautier et al., 2014; Saldi et al., 2009; Schott et al., 2009), it is unlikely that precipitation kinetics have a significant effect on the Mg isotope composition of low temperature magnesite.

Mg isotope fractionation during precipitation of hydrothermal Mg-carbonates in this study (~ -0.5 ‰; estimated as $\Delta^{26}Mg_{carb\text{-}fluid} = \delta^{26}Mg_{carb} - \delta^{26}Mg_{fluid}$ with $\delta^{26}Mg_{fluid} \approx \delta^{26}Mg_{peridotite}$) is slightly smaller but generally consistent with previous estimates based on hydrothermal magnesite in talc-carbonate rock (Beinlich et al., 2014) and high temperature precipitation experiments (Pearce et al., 2012; Schott et al., 2016). Considering a formation temperature of 200 °C for hydrothermal magnesite from Piedmont there is also good agreement with the first principle calculations by Pinilla et al., (2015) and Rustad et al., (2010; Fig. 7).

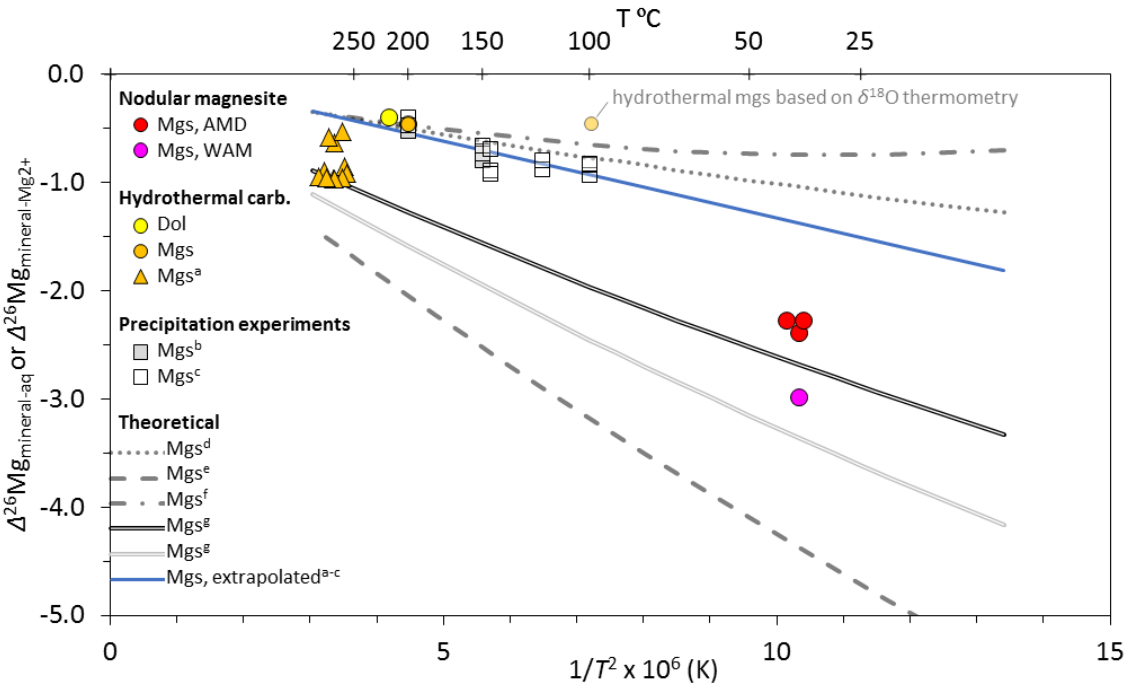

Fig. 7 Mg isotope fractionation between Mg-carbonate and fluid or Mg^{2+} relative to precipitation temperature. Dashed, dotted, dash-dotted and grey ($1Mg30H_2O$) and black ($1Mg50H_2O$) double lines and boxes represent first-principle calculations of $\Delta^{26}Mg_{mgs\text{-}fluid}$ and $\Delta^{26}Mg_{mgs\text{-}fluid}$ of precipitation experiments in the absence of organic ligands at temperatures between 100 °C and 200 °C, respectively. [a]Beinlich et al., (2014); [b]Pearce et al., (2012); [c]Schott et al., (2016); [d]Rustad et al., (2010); [e]Schauble (2011); [f]Pinilla et al., (2015); [g]Wang et al., (2019). The $\delta^{26}Mg$ of weathering and hydrothermal fluids precipitating magnesite and dolomite is assumed to be -0.28 ‰ and -0.23 ‰, respectively. The solid blue line (slope = -0.1421, intercept = 0.0944) represents a linear extrapolation of $\Delta^{26}Mg_{mgs\text{-}Mg2+}$ determined in precipitation experiments (Pearce et al., 2012; Schott et al., 2016) to lower temperature.

The most recent calculations of Mg isotope fractionation between aqueous Mg and magnesite (Wang et al., 2019) agree well with the fractionation documented for some natural samples at high (Beinlich et al., 2014) and low temperatures (this study). However, the consistency of Mg isotope fractionation observed in precipitation experiments (Pearce et al., 2012; Schott et al., 2016), high temperature natural samples (Beinlich et al., 2014; this study) and calculations (Pinilla et al., 2015; Rustad et al., 2010) suggest that the temperature dependence of Mg-isotope fractionation during magnesite precipitation may be rather small compared to predictions by Schauble (2011) or Wang et al., (2019). This is also consistent with previous studies that found no correlation between fluid temperatures and δ^{26}Mg of hydrothermal dolomites formed between ~ 50 °C and 350 °C, suggesting that temperature-dependent Mg-isotope fractionation may be present but obscured by other factors such as differences in fluid source characteristics, dissolution/re-precipitation or diagenetic overprinting (Geske et al., 2015a, Walter et al., 2015). Furthermore, the temperature dependence of Mg isotope fractionation predicted by precipitation experiment (e.g. 0.4 ‰/100 °C) is small compared to the variation of $\delta^{26}Mg_{magnesite}$ at a given temperature, e.g. 0.44 ‰ at 270 ° C (Beinlich et al. 2014) or 0.71 ‰ at 41 °C (this study). Despite the significantly larger Mg isotope fractionation during low-temperature formation of nodular magnesite compared to hydrothermal magnesite, the above indicates that under hydrothermal conditions the δ^{26}Mg of magnesite can only be weakly related to differences in formation temperature.

The study site is hosted in a serpentinite ridge, which has been subjected to uplift at least into the Neogene and its textures reflect weathering rather than burial and diagenesis (Oskierski et al., 2013b; Vickery et al., 2010). Overprinting of Mg isotope signatures of the magnesite due to diagenetic alteration (Fantle and Higgins, 2014; Geske et al., 2012; 2015a; Mavromatis et al., 2014b) is thus considered as insignificant.

5.5.4.Mg-isotope fractionation during low temperature magnesite formation

The δ^{26}Mg of the nodular magnesite investigated in this study is lower than any previously reported (Beinlich et al., 2014; 2018; Dong et al., 2016), suggesting that magnesite formation during

ultramafic rock weathering represents boundary conditions for Mg isotope fractionation during carbonate formation. Similar enrichment of ^{24}Mg in dolomite has been interpreted to result from a complex interplay of different Mg sources and sinks, dissolution/re-precipitation processes, non-equilibrium fractionation processes and overprinting during diagenetic alteration (Geske et al., 2015). As opposed to dolomite, nodular magnesite in this study forms from the weathering of ultramafic rocks or carbonates in silica carbonate rock, both representing proximal and isotopically homogeneous sources of Mg. The main sinks for Mg in the study area, Mg-bearing clay minerals and nodular magnesite forming during weathering, have been identified and isotopically characterised in the present study. Due to the slow precipitation rates of magnesite and the tectonic uplift of the study area, kinetic effects during magnesite precipitation and overprinting during diagenesis can be reasonably excluded as major factors influencing the Mg-isotope composition of nodular magnesite.

Mg isotope fractionation during hydrothermal alteration and subsequent preferential weathering of ^{24}Mg enriched magnesite from pre-existing silica carbonate rock could provide an additional source of ^{24}Mg. Predictions based on $\delta^{26}Mg_{fluid}$ of -0.66 ‰ (the average composition of magnesite and dolomite in silica-carbonate rock) and the extrapolated fractionation factor for magnesite precipitation at 38 °C ($\Delta^{26}Mg_{mgs\text{-}Mg2+}$ ~ -1.4 ‰, blue line in Fig. 7, based on extrapolation of high temperature precipitation experiments) yield a $\delta^{26}Mg_{mgs,}$ of ~ -2.06 ‰, which is higher than the observed Mg isotope compositions of nodular magnesite (-3.26 ‰ < $\delta^{26}Mg_{mgs}$ < -2.55 ‰). As indicated by abundant microporosity in the magnesite (Fig. A2), further enrichment of ^{24}Mg in the nodular magnesite may result from dissolution and re-precipitation of a hydromagnesite precursor. Similarly, formation of calcite and dolomite can occur via amorphous or poorly-ordered precursor phases (Li et al., 2015; Mavromatis et al., 2017a). Considering the fractionation factor for precipitation of hydromagnesite (average $\Delta^{26}Mg_{hmgs\text{-}fluid}$ ~ -1.0 ‰; Shirokova et al., 2013) together with the extrapolated equilibrium fractionation factor for magnesite precipitation at 38 °C ($\Delta^{26}Mg_{mgs\text{-}Mg2+}$ ~ -1.4 ‰) results in overall fractionation ($\Delta^{26}Mg_{mgs\text{-}fluid}$) of ~ -2.4 ‰. The observed Mg isotope composition of nodular magnesite (-3.26 ‰ < $\delta^{26}Mg_{mgs}$ < -2.55 ‰) can then be reconciled with both weathering of ultramafic rocks ($\delta^{26}Mg$ ~ -0.28 ‰) or carbonates in the silica carbonate rock ($\delta^{26}Mg$ ~

-0.66 ‰) as the dominant source of Mg, resulting in predicted $\delta^{26}Mg_{mgs}$ of ~ -2.68 ‰ and -3.06 ‰, respectively.

In addition, the high alkalinity in ultramafic rock weathering fluids (Beinlich and Austrheim, 2012; Oskierski et al., 2016) suggests that inter-species Mg isotope fractionation contributes to enrichment of ^{24}Mg in the nodular magnesite. Superimposing inter-species Mg isotope fractionation ($\delta^{26}Mg_{aq} - \delta^{26}Mg_{Mg2+}$ ~ 1.4 ‰) on the predicted equilibrium fractionation between magnesite and Mg^{2+} at 38 ºC ($\Delta^{26}Mg_{mgs\text{-}Mg2+}$ ~ -0.8 ‰, Pinilla et al., 2015; $\Delta^{26}Mg_{mgs\text{-}Mg2+}$ ~ -1.4 ‰, based on extrapolation of precipitation experiments) results in overall fractionation ($\Delta^{26}Mg_{mgs\text{-}aq}$) between ~ -2.8 ‰ and ~ -2.2 ‰, generally consistent with our observations (Fig. 7). The stronger enrichment in ^{24}Mg of nodular magnesite relative to hydrothermal magnesite, suggests that inter-species Mg isotope fractionation is larger in weathering fluids, consistent with dissolution and re-precipitation of pre-existing carbonate phases leading to higher alkalinity in these fluids. In the absence of Mg source heterogeneity, kinetic isotope effect and diagenetic overprinting, the extreme enrichment of ^{24}Mg in nodular magnesite can only be accounted for if the formation of low temperature, nodular magnesite includes multiple Mg isotope fractionation steps resulting from carbonate dissolution/re-precipitation processes and the related enhanced isotope fractionation between aqueous Mg species in low temperature weathering solutions.

6. Implications for the interpretation of Mg fractionation pathways

The observed ^{26}Mg enrichment of secondary silicate phases during weathering has been documented previously for mafic rocks (Huang et al., 2012; Liu et al., 2014; Teng et al., 2010b) and for hydrothermal alteration of ultramafic rocks (Beinlich et al., 2014; 2018). Along with preferential dissolution of isotopically light carbonate rocks this implies that aqueous Mg in surface and shallow crustal fluid systems will be dominated by the ^{24}Mg isotope, which is consistent with the composition of continental runoff ($\delta^{26}Mg_{runoff}$ = -1.09 ‰, Tipper et al., 2006a; Fig. 4). Mineralogically controlled Mg isotope fractionation during formation of secondary silicates also determines the isotopic

composition of authigenic clay forming on the seafloor, an important sink for Mg in the marine Mg cycle ($\delta^{26}Mg_{seawater}$ = -0.82 ‰, Dunlea et al., 2017; Higgins and Schrag, 2015; Ling et al., 2011; Tipper et al., 2006a, b). Similarly, surface weathering causes ^{26}Mg enrichment in the weathering residual, producing Mg-isotope signatures that appear long lasting and robust during subsequent deep burial, potential fluid alteration and partial melting (Shen et al., 2009; Teng et al., 2016; Wang et al., 2017). Concomitant formation of secondary Mg carbonate appears in some cases to balance ^{26}Mg uptake in secondary silicate phases (Beinlich et al., 2014), while precipitation of ^{24}Mg enriched carbonate during open system alteration will alter the composition of the weathering runoff, thus contributing to the variability of measured Mg isotope ratios in natural continental waters (Tipper et al., 2006b; Zhang et al., 2018).

Both hydrothermal alteration and low-temperature weathering result in fractionation of Mg isotopes into ^{26}Mg enriched secondary silicate and ^{24}Mg enriched carbonate phases (Fig. 4). The distinct Mg-isotope signatures of Mg-silicate and Mg-carbonate minerals have previously been used to distinguish changing weathering regimes (Immenhauser et al., 2010; Kasemann et al. 2014; Tipper et al., 2006b), to infer the evolution of groundwater (Zhang et al. 2018) and to identify the formation of Mg clay rather than Mg-carbonate during subsurface interactions of CO_2–bearing fluids with basalt at the CarbFix site (Oelkers et al., 2019). The latter study highlights the importance of understanding the fate of Mg during CO_2 sequestration in mafic and ultramafic rocks, as the formation of Mg-clay (as opposed to Mg-carbonate) does not lead to the desired storage of CO_2 in carbonate minerals. Similarly, net CO_2 sequestration in ultramafic mine tailings is limited if part of the Mg is recycled from pre-existing Mg-carbonates, rather than from Mg-silicates or oxides (Oskierski et al., 2013; 2016; Turvey et al., 2018; Wilson et al., 2009; 2014). Our data, especially the extreme enrichment of ^{24}Mg in nodular magnesite that is reported here for the first time, thus contributes to a framework for interpreting Mg isotope signatures as a tracer for the sources and fate of Mg during carbonation of ultramafic rocks.

Furthermore, our data show distinct Mg isotope signatures of low-temperature ultramafic-hosted magnesite relative to hydrothermal magnesite, demonstrating the potential to distinguish

magnesite formation pathways or environments based on δ^{26}Mg. Ultramafic-hosted deposits of nodular, cryptocrystalline magnesite (Kraubath-type, see Pohl, 1989, and sources therein for classification) can generally be distinguished from hydrothermal magnesite (Greiner-type) based on grainsize but this is not possible for intermediate deposits with cryptocrystalline magnesite formed at higher temperature (e.g. Piedmont deposit; Ashley, 1995) or cryptocrystalline, sediment-hosted deposits (Bela Stena-type, e.g. Bandalup magnesite deposit, Abeysinghe, 1996). Kraubath-type magnesite forms at low temperatures from meteoric waters (Garcia del Real et al., 2016) but hypogene textures such as meter-sized veins and intense brecciation are also observed (Oskierski et al., 2013b; Quesnel et al., 2016). The extreme enrichment of ^{24}Mg in nodular magnesite with respect to the homogeneous and proximal source of Mg and relative to hydrothermal magnesite suggests that Mg isotope signatures in nodular magnesite record Mg isotope fractionation due to dissolution/re-precipitation processes. Hence, the documented Mg isotope signatures provide an explanation for both supergene and hypogene features leading to a unifying genetic model for Kraubath-type magnesite deposits.

7. Concluding remarks

We document Mg isotope fractionation associated with continental weathering and low-temperature carbonation of ultramafic rocks. The enrichment of ^{26}Mg in weathering products relative to the fresh ultramafic rock concurs with the degree of weathering and is accompanied by loss of MgO as well as increasing clay content in the saprolite. Retention of ^{26}Mg in the structure of secondary Mg-bearing clay minerals is thus controlling the Mg isotope signature of the saprolite, consistent with preferential mobilisation of ^{24}Mg into weathering fluids. Nodular, low temperature magnesite is significantly more enriched in ^{24}Mg than hydrothermal magnesite from the study area, with the lowest δ^{26}Mg documented for magnesite so far. A multiple-step formation pathway involving dissolution re-precipitation of pre-existing magnesite or hydromagnesite associated with inter-species Mg isotope fractionation in alkaline ultramafic rock weathering fluids is required to reconcile the

strong enrichment of ^{24}Mg in nodular, low temperature magnesite with the homogeneous and proximal ultramafic source of Mg. The presented data underpin the ability of Mg isotope signatures to record low temperature alteration processes and highlight the insights that Mg isotope signatures provide into the fate of Mg during carbonation of ultramafic rocks and magnesite genesis.

Acknowledgements

We would like to thank Professor P.M. Ashley for access to some of the samples used in this study. Dr A. Deditius is thanked for insightful discussions of the manuscript. HCO would like to thank the School of Engineering and IT, Murdoch University, for financial support via a NSSG grant. The authors acknowledge the facilities, and the scientific and technical assistance of the Australian Microscopy & Microanalysis Research Facility at the Centre for Microscopy, Characterisation & Analysis, The University of Western Australia, a facility funded by the University, State and Commonwealth Governments. This work has been financially supported by the French national programmes INSU-LEFE and INSU-SYSTER.

References

Abeysinghe P.E., (1996) Talc, pyrophyllite and magnesite in Western Australia. Western Australia Geol Surv., Mineral Res. Bul. 16.

Aharon P. (1988) A stable-isotope study of magnesite from the Rum Jungle Uranium Field, Australia: Implications for the origin of strata-bound massive magnesites. Chem. Geol. 69, 127-145.

Aitchison J.C., Ireland T. R. (1995) Age profile of ophiolitic rocks across the late Paleozoic New England Orogen, New South Wales: implications for tectonic models. Aust. J. Earth Sci. 42, 11–23.

Aitchison J.C., Blake, Jr., M.C., Flood P.G., Murchey B.L. (1988) New and revised lithostratigraphic units from the southwestern New England Fold Belt. Geol. Surv. NSW Quart. Notes 72, 10–16.

Andrews J.E., Stamatakis M.G., Mitsis I., Donnelly T., Regueiroy Gonzalez-Barros M., Fallick A.E. (2018) Stable isotope evidence for near-surface, low-temperature formation of Mg-(hydro)carbonates in highly altered Greek Mesozoic serpentinites. J. Geol. Soc. **175**, 361-375.

Ashley P.M., Brownlow J.W. (1993) Silica-carbonate alteration zones in the Great Serpentinite Belt, southern New England Orogen: their nature and significance, In New England Orogen, (eds. P. G. Flood and J. C. Aitchison). University of New England, Armidale, Australia. pp. 197–214.

Ashley P.M. (1997) Silica-carbonate alteration zones and gold mineralisation in the Great Serpentinite Belt, New England Orogen, New South Wales. In: PM, A., PG, F. (Eds.), *Tectonics and Metallogenesis of the New England Orogen.* Geol. Soc. Aust. Spec. Pub. **19**, pp. 212–225.

Ashley P. M. (1995) The Piedmont hydrothermal magnesite deposit, Great Serpentinite Belt, northern NSW: geochemical and stable isotopic constraints. Research Report 1993–94, Centre for Isotope Studies North Ryde, NSW, Australia. pp. 12–18.

Bales R.C., Morgan J.J. (1985) Dissolution kinetics of chrysotile at pH 7 to 10. Geochim. Cosmochim. Acta 49 (11), 2281–2288.

Beinlich A., Austrheim H., Glodny J., Erambert M., Andersen T.B. (2010) CO_2 sequestration and extreme Mg depletion in serpentinized peridotite clasts from the Devonian Solund basin, SW-Norway. Geochim. Cosmochim. Acta **74**, 6935-6964.

Beinlich A., Austrheim H. (2012) In situ sequestration of atmospheric CO_2 at low temperature and surface cracking of serpentinized peridotite in mine shafts. Chem. Geol. **332-333**, 32-44.

Beinlich A., Mavromatis V., Austrheim H., Oelkers E.H. (2014) Inter-mineral Mg isotope fractionation during hydrothermal ultramafic rock alteration–Implications for the global Mg-cycle. Earth Planet. Sci. Lett. **392**, 166–176.

Beinlich A., Austrheim H., Mavromatis V., Grguric B., Putnis C.V., Putnis A. (2018) Peridotite weathering is the missing ingredient of Earth's continental crust composition. Nature Comm. **9**, No. 634.

Brewer A., Teng F.-Z., Dethier D. (2018) Magnesium isotope fractionation during granite weathering. Chem. Geol. **501**, 95-103.

Brownlow J.W., Ashley P.M. (1991) Piedmont magnesite deposit – a hydrothermal vein system in the Great Serpentinite Belt. Geol. Surv. NSW Quart. Notes 82, 1–20.

Caillaud J., Proust D., Righi D. (2006) Weathering sequence of rock-forming minerals in a serpentinite: influence of microsystems on clay mineralogy. Clay Clay Min. **54-1**, 87-100.

Cawood P.A., Pisarevsky S.A. and Leitch E.C. (2011) Unraveling the New England orocline, east Gondwana accretionary margin. Tectonics 30, TC5002, http://dx.doi.org/10.1029/2011TC002864.

Cross K.C. (1983) The Pigna Barney ophiolitic complex and associated basaltic rocks, northeastern New South Wales, Australia. PhD thesis, University of New England, Australia.

Das Sharma S., Patil D. T., Gopalan K. (2002) Temperature dependence of oxygen isotope fractionation of CO_2 from magnesite–phosphoric acid reaction. Geochim. Cosmochim. Acta **66**, 589–593.

Dauphas N., Teng F.-Z., Arndt N.T. (2010) Magnesium and iron isotopes in 2.7 Ga Alexo komatiites: Mantle signatures, no evidence for Soret diffusion, and identification of diffusive transport in zoned olivine. Geochim. Cosmochim. Acta **74**, 3274-3291.

Dessert C., Dupre B., Gaillardet J., Francois L.M., Allegre C. J. (2003) Basalt weathering laws and the impact of basalt weathering on the global carbon cycle. Chem. Geol. **202**, 257-273.

Di Lorenzo F., Rodriguez-Galan R.M., Prieto M. (2014) Kinetics of the solvent-mediated transformation of hydromagnesite into magnesite at different temperatures. Mineral. Mag. **78-6**, 1363-1372

Dickson B.L., Scott K.M. (1998) Recognitions of Aeolian soils of the Blayney district, NSW: implications for mineral exploration. J. Geochem. Explor. **63**, 237-251.

Dong A., Zhu X.-K., Li S.-Z., Kendall B., Wang Y., Gao Z. (2016) Genesis of a giant Paleoproterozoic strata-bound magnesite deposit: Constraints from Mg isotopes. Precambrian Res. **281**, 673-683.

Dunlea A.G., Murray R.W., Santiago Ramos D.P., Higgins J.A. (2017) Cenozoic global cooling and increased seawater Mg/Ca via reduced reverse weathering. Nature Comms. **8**. 844.

Fantle M.S., Higgins J. (2014) The effects of diagenesis and dolomitization on Ca and Mg isotopes in marine platform carbonates: Implications for the geochemical cycles of Ca and Mg. Geochim. Cosmochim. Acta **142**, 458–481279.

Gautier Q., Benezeth P., Mavromatis V., Schott J. (2014) Hydromagnesite solubility product and growth kinetics in aqueous solution from 25 to 75 °C. Geochim. Cosmochim. Acta **138**, 1-20.

Garcia del Real P., Maher K., Kluge T., Bird D.K., Brown Jr. G.E., John C.M. (2016) Clumped-isotope thermometry of magnesium carbonates in ultramafic rocks. Geochim. Cosmochim. Acta **193**, 222-250.

Geske A., Zorlu J., Richter D.K., Buhl D., Niedermayr A., Immenhauser A. (2012) Impact of diagenesis and low grade metamorphosis on isotope (δ^{26}Mg, δ^{13}C, δ^{18}O and ^{87}Sr/^{86}Sr) and elemental (Ca, Mg, Mn, Fe and Sr) signatures of Triassic sabkha dolomites. Chem. Geol. **332**, 45–64

Geske A., Goldstein R. H., Mavromatis V., Richter D.K., Buhl D., Kluge T., John C.M., Immenhauser A. (2015a) The magnesium isotope (δ^{26}Mg) signature of dolomites. Geochim. Cosmochim. Acta **149**, 131–151.

Geske A., Lokier S., Dietzel M., Richter D.K., Buhl D., Immenhauser A. (2015b) Magnesium isotope composition of sabkha porewater and related (Sub-) recent stoichiometric dolomites, Abu Dhabi (UAE). Chem. Geol. **393– 394**, 112–124.

Hänchen M., Prigiobbe V., Baciocchi R., Mazzotti M. (2008) Precipitation in the Mg-carbonate system - effects of temperature and CO_2 pressure. Chem. Eng. Sci., **63-4**, 1012-1028.

Harrison A. L., Dipple G. M., Song W., Power I. M., Mayer K. U., Beinlich A., Sinton D. (2017) Changes in mineral reactivity driven by pore fluid mobility in partially wetted porous media. Chem. Geol. **463**, 1-11.

Harrison A.L., Mavromatis V., Oelkers E.H., Benezeth P. (2019) Solubility of the hydrated Mg-carbonates nesquehonite and dypingite from 5 to 35 ºC: Implications for CO_2 storage and the relative stability of Mg-carbonates. Chem. Geol. 504, 123-135.

Higgins J. A., Schrag D. P. (2015) The Mg isotopic composition of Cenozoic seawater – evidence for a link between Mg-clays, seawater Mg/Ca, and climate. Earth Planet. Sci. Lett. **416**, 73-81.

Hin R.C., Coath C.D., Carter P.J., Nimmo F., Lai Y.J., Pogge von Strandmann P.A.E., Willbold M., Leinhardt Z.M., Walter M.J., Elliott T. (2017) Magnesium isotope evidence that accretional vapour loss shapes planetary compositions. Nature **549**, 511.

Hollingberry L.A., Hull T.R. (2010) The thermal decomposition of huntite and hydromagnesite – A review. Thermochim. Acta **509**, 1-11.

Huang K.J., Teng F.Z., Wei G.J., Ma J.L., Bao Z.Y. (2012) Adsorption- and desorption-controlled magnesium isotope fractionation during extreme weathering of basalt in Hainan Island, China. Earth Planet. Sci. Lett. **359**, 73–83.

Immenhauser A., Buhl D., Richter D., Niedermayr A., Riechelmann D., Dietzel M., Schulte U. (2010). Magnesium-isotope fractionation during low-Mg calcite precipitation in a limestone cave—Field study and experiments. Geochim. Cosmochim. Acta **74**, 4346–4364.

Kasemann S.A., Pogge von Strandmann P.A.E, Prave A.r., Fallick A.E., Elliott T., Hoffman K.-H. (2014) Continental weathering following a Cryogenian glaciation: Evidence from calcium and magnesium isotopes. Earth Plant. Sci. Lett. 396, 66-77.

Kralik M., Aharon P., Schroll E., Zachmann D. (1989) Carbon and oxygen isotope systematics of magnesite: a review. In: Möller, P. (Ed.), *Magnesite*. Monogr. Ser. Min. Depos. **28**, pp. 197–223.

Kelemen P.B., Matter J., Streit E.E., Rudge J.F., Curry, W.B., Blusztajn J. (2011) Mineral carbonation in peridotite: Natural processes and recipes for enhanced, in situ CO_2 capture and storage. Annu. Rev. Earth Planet. Sci. **39**, 545-576.

Königsberger E., Königsberger L., Gamsjager H. (1999) Low-temperature thermodynamic model for the system Na_2CO_3-$MgCO_3$-$CaCO_3$-H_2O. Geochim. Cosmochim. Acta **63**, 3105-3119.

Lai Y.-J., Pogge von Strandmann P.A.E., Dohmen R., Takazawa E., Elliott T. (2015) The influence of melt infiltration on the Li and Mg isotopic composition of the Horoman Peridotite Massif. Geochim. Cosmochim. Acta **164**, 318-332.

Lara M.C., Buss H.L., Pogge von Strandmann P.A.E., Schüssler J.A., Moore O.W. (2017) The influence of critical zone processes on the Mg isotope budget in a tropical, highly weathered andesitic catchment. Geochim. Cosmochim. Acta **201**, 77-100.

Li W.Y., Teng F.-Z., Xiao Y., Huang J. (2011) High-temperature inter-mineral magnesium isotope fractionation in eclogite from the Dabie Shan orogen, China. Earth Planet. Sci. Lett. **304**, 224–230.

Li W., Chakraborty S., Beard B.L., Romanek C.S., Johnson C.M. (2012) Magnesium isotope fractionation during precipitation of inorganic calcite under laboratory conditions. Earth Planet. Sci. Lett. **333-334**, 304-216.

Li W., Beard B.L., Li C., Johnson C.M. (2014) Magnesium isotope fractionation between brucite [$Mg(OH)_2$] and Mg aqueous species: Implications for silicate weathering and biogeochemical processes. Earth Planet. Sci. Lett., **394**, 82-93.

Li W., Beard B.L., Li C., Xu H., Johnson C.M. (2015) Experimental calibration of Mg isotope fractionation between dolomite and aqueous solution and its geological implications. Geochim. Cosmochim. Acta **157**, 164-181.

Ling M. X., Sedaghatpour F., Teng F.Z., Hays P.D., Strauss J., Sun W.D. (2011) Homogeneous magnesium isotopic composition of seawater: An excellent geostandard for Mg isotope analysis. Rapid Commun. Mass Spectrom. **25**, 2828–2836.

Liu S.A., Teng F.-Z., He Y.S., Ke S., Li S.G. (2010a) Investigation of magnesium isotope fractionation during granite differentiation: Implication for Mg isotopic composition of the continental crust. Earth Planet. Sci. Lett. **297**, 646–654.

Liu J., Fu G., Song X., Charles S.P., Zhang Y., Han D., Wang S. (2010b) Stable isotopic composition in Australian precipitation. J. Geophys. Res. **115**, D23307.

Liu X.-M., Teng F.-Z., Rudnick R.L., McDonough W.F., Cummings M. (2014) Massive magnesium depletion and isotopic fractionation in weathered basalts. Geochim. Cosmochim. Acta, **135**, 336–349.

Liu P.-P., Teng F.-Z., Dick H.J.B., Zhou M.F., Chung S.-L. (2017) Magnesium isotopic composition of the oceanic mantle and oceanic Mg cycling. Geochim. Cosmochim. Acta **206**, 151-165.

Mavromatis V., Gautier Q., Bosc O., Schott J. (2013) Kinetics of Mg partition and Mg stable isotope fractionation during its incorporation in calcite. Geochim. Cosmochim. Acta **114**, 188–203.

Mavromatis V., Pearce C.R., Shirokova L.S., Bundeleva I.A., Pokrovsky O.S., Benezeth P., Oelkers E.H. (2012) Magnesium isotope fractionation during hydrous magnesium carbonate precipitation with and without cyanobacteria. Geochim. Cosmochim. Acta **76**, 161–174.

Mavromatis, V., Prokushkin, A.S., Pokrovsky, O.S., Viers, J., Korets, M.A. (2014a) Magnesium isotopes in permafrost-dominated Central Siberian larch forest watersheds. Geochim. Cosmochim. Acta147, 76–89.

Mavromatis V., Meister P., Oelkers E.H. (2014b) Using stable Mg isotopes to distinguish dolomite formation mechanisms: A case study from the Peru Margin. Chem. Geol. **385**, 84–91.

Mavromatis V., Rinder T., Prokushkin A.S., Pokrovsky O.S., Korets M.A., Chmeleff J., Oelkers E.H. (2016) The effect of permafrost, vegetation, and lithology on Mg and Si isotope composition of the Yenisey River and its tributaries at the end of the spring flood. Geochim. Cosmochim. Acta **191**, 32-46.

Mavromatis V., Purgstaller B., Dietzel M., Buhl D., Immenhauser A., Schott J. (2017a) Impact of amorphous precursor phase on magnesium isotope signatures of Mg-calcite. Earth Planet. Sci. Let. **464**, 227-236.

Mavromatis V., Immenhauser A., Buhl D., Purgstaller B., Baldermann A., Dietzel M. (2017b) Effect of organic ligands on Mg partitioning and Mg isotope fractionation during low-temperature precipitation of calcite in the absence of growth rate effects. Geochim. Cosmochim. Acta **207**, 139-153.

Oelkers E. H., Benning L. G., Lutz S., Mavromatis V., Pearce C. R. and Plumper O. (2015) The efficient long-term inhibition of forsterite dissolution by common soil bacteria and fungi at Earth surface conditions. Geochim. Cosmochim. Acta 168, 222–235.

Oelkers E.H., Berninger U.N., Perez-Fernandez A., Chmeleff J., Mavromatis V. (2018) The temporal evolution of magnesium isotope fractionation during hydromagnesite dissolution, precipitation, and at equilibrium. Geochem. Cosmochim. Acta **226**, 36-49.

Oelkers E.H., Butcher R., Pogge von Strandmann P.A.E., Schuessler J.A., von Blanckenburg F., Snaebjoernsdottir S.A., Mesfin K., Aradottir E.S., Gunnarson I., Sigfusson B., Gunnlaugsson E., Matter J.M., Stute M., Gislason S.R. (2019) Using stable Mg isotopes signatures to assess the fate of magnesium during the in situ mineralization of CO_2 and H_2S at the CarbFix site in SW-Iceland. Geochim. Cosmochim. Acta **245**, 542-555.

Opfergelt S., Georg R.B., Delvaux B., Cabidoche Y.M., Burton K.W., Halliday A.N. (2012) Mechanisms of magnesium isotope fractionation in volcanic soil weathering sequences, Guadeloupe. Earth Planet. Sci. Lett. **341**, 176–185

Opfergelt S., Burton K.W., Georg R.B., West A.J., Guicharnaud R.A., Sigfusson B., Siebert C., Gislason S.R., Halliday A.N. (2014) Magnesium retention on the soil exchange complex controlling Mg isotope variations in soils, soil solutions and vegetation in volcanic soils, Iceland. Geochim. Cosmochim. Acta **125**, 110–130.

Oskierski H.C., Bailey J.G., Kennedy E.M., Jacobsen G., Ashley P.M., Dlugogorski B.Z. (2013a) Formation of weathering-derived magnesite deposits in the New England Orogen, New South Wales, Australia: Implications from mineralogy, geochemistry and genesis of the Attunga Magnesite Deposit. Mineralium Deposita **48**, 525-541.

Oskierski H.C., Dlugogorski B.Z., Jacobsen G. (2013b) Sequestration of atmospheric CO_2 in a weathering-derived, serpentinite-hosted magnesite deposit: ^{14}C tracing of carbon sources and age constraints for a refined genetic model. Geochim. Cosmochim. Acta **122**, 226-246.

Oskierski H.C., Dlugogorski B.Z., Jacobsen G. (2013c) Sequestration of atmospheric CO_2 in chrysotile mine tailings of the Woodsreef Asbestos Mine, Australia: Quantitative mineralogy, isotopic fingerprinting and carbonation rates. Chem. Geol. **358**, 156-169.

Oskierski H.C., Dlugogorski B.Z., Oliver T.K., Jacobsen G. (2016) Chemical and isotopic signatures of waters associated with the carbonation of ultramafic mine tailings, Woodsreef Asbestos Mine, Australia. Chem. Geol., **436**, 11-23.

Oskierski H.C. (2013) Natural carbonation of ultramafic rocks in the Great Serpentinite Belt, New South Wales, Australia. Ph.D. thesis, The University of Newcastle, Australia.

Palmer D. A., Wesolowski D. J. (1997) Potentiometric measurements of the first hydrolysis constant of magnesium (II) to 250 _C and 5 molal ionic strength (NaCl). J. Solut. Chem. 26, 217–232.

Parkhurst D.L., Appelo C.A.J. (2013) Description of input and examples for PHREEQC version 3—A computer program for speciation, batch-reaction, one-dimensional transport, and inverse geochemical calculations: U.S. Geol. Surv. Techniques Methods 6, A43, 497 p., http://pubs.usgs.gov/tm/06/a43/.

Pearce C.R., Saldi G.D., Schott J., Oelkers E.H. (2012) Isotopic fractionation during congruent dissolution, precipitation and at equilibrium: Evidence from Mg isotopes. Geochim. Cosmochim. Acta **92**, 170–183.

Perez Fernandez A., Berninger U.N., Mavromatis V., Pogge von Strandmann P.A.E., Oelkers E.H. (2017) Ca and Mg isotope fractionation during the stoichiometric dissolution of dolomite at temperatures from 51 to 126 ºC and 5 bars CO2 pressure. Chem. Geol. **467**, 76-88.

Pinilla C., Blanchard M., Balan E., Suresh K., Natarajan S.K., Vuilleumier R., Mauri F. (2015) Equilibrium magnesium isotope fractionation between aqueous Mg^{2+} and carbonate minerals: insights from path integral molecular dynamics. Geochim. Cosmochim. Acta **163**, 126–139.

Pogge von Strandmann P.A.E., Burton K.W., James R.H., van Calsteren P., Gislason S.R., Sigfusson B. (2008) The influence of weathering processes on riverine magnesium isotopes in a basaltic terrain. Earth Planet. Sci. Lett. **276**, 187–197.

Pogge von Strandmann P.A.E., Opfergelt S., Lai Y.-J., Sigfusson B., Gislason S.R., Burton K. W. (2012) Lithium, magnesium and silicon isotope behaviour accompanying weathering in a basaltic soil and pore water profile in Iceland. Earth Planet. Sci. Lett. **339-340**, 11-23.

Pohl, W. (1989) Comparative geology of magnesite deposits and occurrences. In: Möller, P. (Ed.), *Magnesite*. Monogr. Ser. Min. Depos. **28**, pp. 1-13.

Pokharel R., Gerrits R., Schuessler J.A., Floor G.H., Gorbushina A.A., von Blanckenburg F. (2017) Mg isotope fractionation during uptake by a rock-inhabiting, model microcolonial fungus knufia petricola at acidic and neutral pH. Environ. Sci. Technol. **51**, 9691-9699.

Pokrovsky B.G., Mavromatis V., Pokrovsky O.S. (2011) Co-variation of Mg and C isotopes in late Precambrian carbonates of the Siberian Platform: A new tool for tracing the change in weathering regime? Chem. Geol. **290**, 67-74.

Pokrovsky O.S., Schott J. (2000) Kinetics and mechanisms of forsterite dissolution at 25 °C and pH from 1 to 12. Geochim. Cosmochim. Acta 64-19, 3313–3325.

Pokrovsky O.S., Golubev S.V., Schott J., Castillo A. (2009) Calcite, dolomite and magnesite dissolution kinetics in aqueous solutions at acid to circumneutral pH, 25 to 150 ° C and 1 to 55 atm pCO2: New constraints on CO_2 sequestration in sedimentary basins. Chem. Geol. 265, 20-32.

Poppe L.J., Paskevich V.J., Hathaway J.C., Blackwood D.S. (2001) A laboratory manual for X-ray powder diffraction. USGS Open-File Report 01-041.

Power I.M., Wilson S.A., Harrison A.L., Dipple G.M., McCutcheon J., Southam G., Kenward P.A. (2014) A depositional model for hydromagnesite-magnesite playas near Atlin, British Columbia, Canada. Sediment. **61**, 1701-1733.

Power I.M., Kenward P.A., Dipple D.M., Raudsepp M. (2017) Room temperature magnesite precipitation. Cryst. Growth Des. **17-11**, 5652-5659.

Power I.M., Harrison A.L., Dipple G.M., Wilson S.A., Barker S.L.L., Fallon S.J. (2019) Magnesite formation in playa environments near Atlin, British Columbia, Canada. Geochim. Cosmochim. Acta 255, 1-24.

Quesnel B., Boulvais P., Gautier P., Cathelineau M., John C.M., Dierick M., Agrinier P., Drouillet M. (2016) Paired stable isotopes (O, C) and clumped isotope thermometry of magnesite and silica veins in the New Caledonia Peridotite Nappe. Geochim. Cosmochim. Acta **183**, 234-249.

Riechelmann S., Mavromatis V., Buhl D., Dietzel M., Eisenhauer A., Immenhauser A. (2016) Impact of diagenetic alteration on brachiopod shell magnesium isotope (δ^{26}Mg) signatures: Experimental versus field data. Chem. Geol. **440**, 191-206.

Riechelmann S., Mavromatis V., Buhl D., Dietzel M., Hoffmann R., Joens N., Kell-Duivenstein I., Immenhauser A. (2018) Echinoid skeletal carbonate as archive of past seawater magnesium isotopes signatures – Potential and limitations. Geochim. Cosmochim. Acta **235**, 333-359.

Rustad J.R., Casey W.H., Yin Q.Z., Bylaska E.J., Felmy A.R., Bogatko S.A., Jackson V.E., Dixon D.A. (2010) Isotopic fractionation of Mg^{2+}(aq), Ca^{2+}(aq), and Fe^{2+}(aq) with carbonate minerals. Geochim. Cosmochim. Acta **74**, 6301–6323.

Ryu J.-S., Jacobsen A.D., Holmden C., Lundstrom C., Zhang Z. (2011) the major ion $\delta^{44/40}$Ca, $\delta^{44/42}$Ca, and $\delta^{26/24}$Mg geochemistry of granite weathering at pH = 1 and T = 25 ° C: power-law processes and the relative reactivity of minerals. Geochim. Cosmochim. Acta 75, 6004-6026.

Ryu J.S., Vigier N., Decarreau A., Lee S.W., Lee K.S., Song H., Petit S. (2016) Experimental investigation of Mg isotope fractionation during mineral dissolution and clay formation. Chem. Geol. 445, 135-145.

Saldi G.D., Kohler S.J., Marty N., Oelkers E.H. (2007) Dissolution rate of talc as a function of solution composition, pH and temperature. Geochim. Cosmochim. Acta 71, 3446-3457.

Saldi G.D., Jordan G., Schott J., Oelkers E.H. (2009) Magnesite growth rates as a function of temperature and saturation state. Geochim. Cosmochim. Acta **73**, 5646–5657.

Schauble E. A. (2011) First-principles estimates of equilibrium magnesium isotope fractionation in silicate, oxide, carbonate and hexaaquamagnesium(2+) crystals. Geochim. Cosmochim. Acta **75**, 844–869.

Schott J., Pokrovsky O.S., Oelkers E.H. (2009) The link between mineral dissolution/precipitation and solution chemistry. Rev. Mineral. Geochem. **70**, 207-258.

Schott J., Mavromatis V., Fujii T., Pearce C.R., Oelkers E.H. (2016) The control of carbonate mineral Mg isotope composition by aqueous speciation: Theoretical and experimental modelling. Chem. Geol. **445**, 120-134.

Shalev N., Farkas J., Fietzke J., Novak M., Schuessler J.A., Pogge von Strandmann P.A.E., Toerbe, P.B. (2018) Mg isotope interlaboratory comparison of reference materials from Earth-surface low-temperature environments. Geostand. Geoanal. Res. **42-2**, 205-221.

Shen B., Jacobsen B., Lee C.-T.A., Yin Q.-Z., Morton D.M. (2009) The Mg isotopic systematics of granitoids in continental arcs and implications for the role of chemical weathering in crust formation. Proc. Natl. Acad. Sci. USA **106**, 20652-20657.

Shirokova L.S., Mavromatis V., Bundeleva I.A., Pokrovsky O.S., Benezeth P., Gerard E., Pearce C.R., Oelkers, E.H. (2013) Using Mg isotopes to trace cyanobacterially mediated magnesium carbonate precipitation in alkaline lakes. Aquat. Geochem. **19**, 1–24.

Skrzypek G. (2013) Normalization procedures and reference material selection in stable HCNOS isotope analyses – an overview. Anal. Bioanal. Chem. **405**, 2815-2823.

Snow J.E., Dick H.J.B. (1995) Pervasive magnesium loss by marine weathering of peridotite. Geochim. Cosmochim. Acta **59**, 4219–4235.

Stefansson A., Benezeth P., Schott J. (2013) Carbonic acid ionization and the stability of sodium bicarbonate and carbonate ion pairs to 200 ° C – A potentiometric and spectrophotometric study. Geochim. Cosmochim. Acta 120, 600–611.

Stefansson A., Benezeth P., Schott J. (2014) Potentiometric and spectrophotometric study of the stability of magnesium carbonate and bicarbonate pairs to 150C and aqueous inorganic carbon speciation and magnesite solubility. Geochim. Cosmochim. Acta 138, 21–31.

Suchet P.A., Probst J.L., Ludwig A. (2003) Worldwide distribution of continental rock lithology: Implications for the atmospheric/soil CO_2 uptake by continental weathering and alkalinity river transport to the oceans. Glob. Biogeochem. Cycles **17**, 1038.

Teng F.-Z., Li W.Y., Rudnick R.L., Gardner L.R. (2010a) Contrasting lithium and magnesium isotope fractionation during continental weathering. Earth Planet. Sci. Lett. **300**, 63–71.

Teng F.-Z., Li W.Y., Ke S., Marty B., Dauphas N., Huang S.C., Wu F.Y., Pourmand A. (2010b) Magnesium isotopic composition of the Earth and chondrites. Geochim. Cosmochim. Acta **74**, 4150–4166.

Teng F.-Z., Hu Y., Chauvel C. (2016) Magnesium isotope geochemistry in arc volcanism. Proc. Natl. Acad. Sci. USA **113**, 7082-7087.

Teng F.-Z. (2017) Magnesium isotope geochemistry. Revs. Min. Petrol. 82, 219-287.

Tipper E.T., Galy A., Gaillardet J., Bickle M.J., Elderfield H., Carder E.A. (2006a) The magnesium isotope budget of the modern ocean: Constraints from riverine magnesium isotope ratios. Earth Planet. Sci. Lett. **250**, 241–253.

Tipper E.T., Galy A., Bickle M.J. (2006b) Riverine evidence for a fractionated reservoir of Ca and Mg on the continents: Implications for the oceanic Ca cycle. Earth Planet. Sci. Lett. **247**, 267–279.

Tipper E.T., Gaillardet J., Louvat P., Capmas F., White A.F. (2010) Mg isotope constraints on soil pore–fluid chemistry: Evidence from Santa Cruz, California. Geochim. Cosmochim. Acta **74**, 3883–3896.

Tipper E.T., Calmels D., Gaillardet J., Louvat P., Capmas F., Dubacq B. (2012a) Positive correlation between Li and Mg isotope ratios in the river waters of the Mackenzie Basin challenges the interpretation of apparent isotopic fractionation during weathering. Earth Planet. Sci. Lett. **333**, 35–45.

Tipper E.T., Lemarchand E., Hindshaw R.S., Reynolds B.C., Bourdon B. (2012b) Seasonal sensitivity of weathering processes: Hints from magnesium isotopes in a glacial stream. Chem. Geol. **312**, 80–92.

Turvey C.C., Wilson S.A., Hamilton J.L., Tait A.W., McCutcheon J., Beinlich A., Fallon S.J., Dipple G.M., Southam G. (2018) Hydrotalcites and hydrated Mg-carbonates as carbon sinks in serpentinite mineral

wastes from the Woodsreef chrysotile mine, New South Wales, Australia: Controls on carbonate mineralogy and efficiency of CO_2 air capture in mine tailings. Int. J. Greenhouse Gas Control **79**, 38-60.

Ulven O. I., Beinlich A., Hövelmann J., Austrheim H., Jamtveit B. (2017) Subarctic physicochemical weathering of serpentinized peridotite. Earth Planet. Sci. Lett. **468**, 11-26.

Van der Beek P., Pulford A., Braun J. (2001) Cenozoic landscape development in the Blue Mountains (SE Australia): lithological and tectonic controls on rifted margin morphology. J. Geol. **109**, 35-56.

Vickery N.M., Brown R.E., Percival I.G. (2010) Manilla 1:100000 Geological Sheet 9036 Explanatory notes. NSW Geol. Surv., Maitland, Australia.

Walter B.F., Immenhauser A., Geske A., Markl G. (2015) Exploration of hydrothermal magnesium isotope signatures as tracers for continental fluid aquifers, Schwarzwald mining district, SW Germany. Chem. Geol. **400**, 87-105.

Wang S.-J., Teng F.-Z., Li S.-G., Zhang L.-F., Du J.-X., He Y.-S., Niu Y. (2017) Tracing subduction zone fluid-rock interactions using trace element and Mg-Sr-Nd isotopes. Lithos 290-291, 94-103.

Wang W., Zhou C., Liu Y., Wu Z., Huang F. (2019) Equilibrium Mg isotope fractionation among aqueous Mg2+, carbonates, brucite and lizardite: Insights from first-principles molecular dynamics simulations. Geochim. Cosmochim. Acta 250, 117-129.

Wilson S.A., Dipple G.M., Power I.M., Thom J.M., Anderson R.G., Raudsepp M., Gabites J.E., Southam G. (2009) Carbon dioxide fixation within mine wastes of ultramafic hosted ore deposits: examples from the Clinton Creek and Cassiar chrysotile deposits, Canada. Econ. Geol. **104**, 95–112.

Wilson S.A., Barker S.L., Dipple G.M., Atudorei V. (2010) Isotopic disequilibrium during uptake of atmospheric CO2 into mine process waters: implications for CO_2 sequestration. Environ. Sci. Technol. 44, 9522–9529.

Wilson S.A., Harrison A.L., Dipple G.M., Power I.M., Barker S.L.L., Mayer K.U., Fallo S.J., Raudsepp M., Southam G. (2014) Offsetting of CO2 emissions by air capture in mine tailings at the Mount Keith nickel mine, Western Australia: rates, controls and prospects for carbon neutral mining. Int. J. Greenhouse Gas Control **25**, 121–140.

Wimpenny J., Gislason S.R., James R.H., Gannoun A., Pogge Von Strandmann P.A.E., Burton K.W. (2010) The behaviour of Li and Mg isotopes during primary phase dissolution and secondary mineral formation in basalt. Geochim. Cosmochim. Acta **74**, 5259–5279.

Wimpenny J., Burton K.W., James R.H., Gannoun A., Mokadem F., Gislason S.R. (2011) The behaviour of magnesium and its isotopes during glacial weathering in an ancient shield terrain in West Greenland. Earth Planet. Sci. Lett. **304**, 260–269

Wimpenny J., Colla C.A, Yin Q.-Z., Rustad J.R., Casey W.H. (2014) Investigating the behaviour of Mg isotopes during the formation of clay minerals. Geochim. Cosmochim. Acta **128**, 178-194.

Wombacher F., Eisenhauer A., Heuser A., Weyer S. (2009) Separation of Mg, Ca and Fe from geological reference materials for stable isotope ratio analyses by MC-ICP-MS and double-spike TIMS. J. Anal. At. Spectrom. 24, 627-636.

Wombacher F., Eisenhauer A., Boehm F., Gussone N., Regenberg M., Dullo W.-C., Rueggeberg A. (2011) Magnesium stable isotope fractionation in marine biogenic calcite and aragonite. Geochim. Cosmochim. Acta **75**, 5797-5818.

Zhang L. (2000) Kinetics and mechanisms of formation of magnesite from hydromagnesite in brine. Technical Report SAN099-19465. Sandia National Laboratories, Albuquerque (NM 87185-0750, USA).

Zhang H., Jiang X.-W., Wan L., Ke S., Liu S.-A., Han G., Guo H., Dong A. (2018) Fractionation of Mg isotopes by clay formation and calcite precipitation in groundwater with long residence times in a sandstone aquifer, Ordos Basin, China. Geochim. Cosmochim. Acta **237**, 261-274.